

Effects of potential field delay and coupling delay on collective behavior of a fractional-order coupled system in a dichotomous fluctuating potential

Yangfan Zhong(钟扬帆), Xi Chen(陈熙), Maokang Luo(罗懋康), and Tao Yu(蔚涛)

Citation: Chin. Phys. B, 2025, 34 (**5**): 050501. DOI: 10.1088/1674-1056/adbd15
Journal homepage: http://cpb.iphy.ac.cn; http://iopscience.iop.org/cpb

What follows is a list of articles you may be interested in

Fractional-order heterogeneous memristive Rulkov neuronal network and its medical image watermarking application

Dawei Ding(丁大为), Yan Niu(牛炎), Hongwei Zhang(张红伟), Zongli Yang(杨宗立), Jin Wang(王金), Wei Wang(王威), and Mouyuan Wang(王谋媛)
Chin. Phys. B, 2024, 33 (**5**): 050503. DOI: 10.1088/1674-1056/ad322b

Dynamics analysis and cryptographic implementation of a fractional-order memristive cellular neural network model

Xinwei Zhou(周新卫), Donghua Jiang(蒋东华), Jean De Dieu Nkapkop, Musheer Ahmad, Jules Tagne Fossi, Nestor Tsafack, and Jianhua Wu(吴建华)
Chin. Phys. B, 2024, 33 (**4**): 040506. DOI: 10.1088/1674-1056/ad03dd

Memory effect in time fractional Schrödinger equation

Chuanjin Zu(祖传金) and Xiangyang Yu(余向阳)
Chin. Phys. B, 2024, 33 (**2**): 020501. DOI: 10.1088/1674-1056/ad02e6

A novel fractional-order hyperchaotic complex system and its synchronization

Mengxin Jin(金孟鑫), Kehui Sun(孙克辉), and Shaobo He(贺少波)
Chin. Phys. B, 2023, 32 (**6**): 060501. DOI: 10.1088/1674-1056/acc0f6

Finite-time synchronization of uncertain fractional-order multi-weighted complex networks with external disturbances via adaptive quantized control

Hongwei Zhang(张红伟), Ran Cheng(程然), and Dawei Ding(丁大为)
Chin. Phys. B, 2022, 31 (**10**): 100504. DOI: 10.1088/1674-1056/ac686b

---

Effects of potential field delay and coupling delay on collective behavior of a fractional-order coupled system in a dichotomous fluctuating potential

Yangfan Zhong(钟扬帆)[1], Xi Chen(陈熙)[3], Maokang Luo(罗懋康)[1,2], and Tao Yu(蔚涛)[1,†]

[1] *College of Mathematics, Sichuan University, Chengdu* 610064, *China*
[2] *College of Aeronautics and Astronautics, Sichuan University, Chengdu* 610064, *China*
[3] *The* 10*th Research Institute of China Electronics Technology Group Corporation, Chengdu* 610066, *China*

(Received 5 December 2024; revised manuscript received 1 February 2025; accepted manuscript online 6 March 2025)

The collective dynamic of a fractional-order globally coupled system with time delays and fluctuating frequency is investigated. The power-law memory of the system is characterized using the Caputo fractional derivative operator. Additionally, time delays in the potential field force and coupling force transmission are both considered. Firstly, based on the delay decoupling formula, combined with statistical mean method and the fractional-order Shapiro–Loginov formula, the "statistic synchronization" among particles is obtained, revealing the statistical equivalence between the mean field behavior of the system and the behavior of individual particles. Due to the existence of the coupling delay, the impact of the coupling force on synchronization exhibits non-monotonic, which is different from the previous monotonic effects. Then, two kinds of theoretical expression of output amplitude gains G and $\bar{G}$ are derived by time-delay decoupling formula and small delay approximation theorem, respectively. Compared to $\bar{G}$, G is an exact theoretical solution, which means that G is not only more accurate in the region of small delay, but also applies to the region of large delay. Finally, the study of the output amplitude gain G and its resonance behavior are explored. Due to the presence of the potential field delay, a new resonance phenomenon termed "periodic resonance" is discovered, which arises from the periodic matching between the potential field delay and the driving frequency. This resonance phenomenon is analyzed qualitatively and quantitatively, uncovering undiscovered characteristics in previous studies.

Keywords: potential field delay, coupling delay, fractional-order, collective behavior

PACS: 05.10.Gg, 05.10.–a, 05.45.Xt, 05.40.–a

DOI: 10.1088/1674-1056/adbd15 **CSTR:** 32038.14.CPB.adbd15

1. Introduction

Stochastic resonance (SR) is a nonlinear phenomenon that enables the enhancement of the signal-to-noise ratio by judiciously introducing noise to the input signal within nonlinear conditions. This phenomenon challenges our conventional perception of noise as a mere disturbance.[1] Since proposed by Benzi *et al.*[2] in 1981, SR has garnered significant attention and has been extensively studied in various disciplines, including physics[3] and biology.[4] The conventional understanding of SR involves the cooperative interplay between periodic forces and noise within a nonlinear system.[2,5–7] However, in 1994, Gammaitoni *et al.*[8] made a significant discovery by observing the SR phenomenon in a multiplicative bistable stochastic system. This breakthrough illustrated the ability of multiplicative noise to introduce a form of effective non-linearity. Subsequently, numerous researchers have explored the occurrence of SR in different linear systems under the influence of multiplicative colored noise, including random damping, mass fluctuation, and fluctuations of the potential energy.[9–12]

There has been a significant amount of research focused on studying SR in single-particle stochastic systems. Over the past few decades, scholars have shown an increasing inclination to investigate the occurrence of SR in coupled stochastic systems.[13,14] This field has gained importance within the broader discipline of nonlinear science. On the one hand, the burgeoning advancement of complex networks has made the investigation of SR in such systems a research hotspot. For example, Nicolis *et al.*[13] conducted an analysis on the spatiotemporal dynamics of nonlinear spatially coupled subsystems, wherein they observed that the inclusion of spatial degrees of freedom leads to significant alterations in the transition mechanisms between states, leading to a pronounced reliance of the response on both the coupling constant and the size of the system. On the other hand, complex networks can exhibit rich collective behaviors[15,16] such as synchronization patterns.[17] Jiang *et al.*[15] focused on exploring collective dynamic behavior within a system of globally connected harmonic oscillators, including synchronization, stability, and SR. Quintero-Quiroz *et al.*[16] conducted a study on the collective behavior of a system comprising chaotic Rossler oscillators. These oscillators were indirectly coupled through a

†Corresponding author. E-mail: scuyutao@163.com

© 2025 Chinese Physical Society and IOP Publishing Ltd. All rights, including for text and data mining, AI training, and similar technologies, are reserved.

shared environment, which had its own dynamics and was further influenced by the interaction with the oscillators. Massihi *et al.*[17] examined how the synchronization of interconnected oscillators is affected by nonlinear coupling.

Time delay, usually reflect the transmission of signal and energy, the limited reaction time, etc.[18–23] The properties of time delay in complex systems have been extensively investigated, including synchronization with time delay,[21,24] SR with delayed interactions,[25,26] and neuronal dynamics with time delays,[27,28] etc. It has been proven that the delay differential equations are powerful mathematical modeling tools in diverse domains, for describing the evolutionary processes that involve the influence of past events.[18] Especially, dynamics behaviors such as chaos, synchronization, and amplitude death in delay coupled system has attracted the attention of numerous researchers.[22,23,29–31] Bernerjee *et al.*[29–31] conducted a systematic investigation into the diverse synchronization scenarios of distinct coupled time delay systems, revealing distinctly characterized chaotic and hyperchaotic oscillations. Besides, Zou *et al.*[22] conducted research on amplitude death in nonlinear oscillators with mixed time-delayed coupling, contributing to a deeper understanding of delay-induced amplitude death in coupled nonlinear oscillators. However, the collective behaviors in delay coupled systems interplaying with noises receive limited attention from scholars. In light of this, we conducted a study on the collective behaviors of a delay coupled stochastic system in Ref. [23]. The analytic solution of output amplitude gain (OAG) is derived by establishing the time delay decoupling formula, and the discussion of collective behaviors, i.e., stability, statistical synchronization, and SR, is given.

However, the model[23] is restricted to the discussion of the integer-order system. For viscoelastic processes, the damping term is influenced not only by the current velocity but also by the past velocity history, as described by fractional-order models, which are better suited for characterizing anomalous diffusion processes.[32] Fractional-order models have gained prominence as a significant asset in diverse domains, encompassing physics, engineering, viscoelastic materials, and other areas.[32–36] And in recent years, the research and interest regarding fractional-order systems with time delay have experienced a significant increase. For example, Lin *et al.*[34] put forward a time-delayed fractional oscillator that experiences damping fluctuations and signal-modulated noise, and explored the occurrence of generalized stochastic resonance phenomena. The inclusion of fractional-order derivatives in coupled systems has also attracted significant scholarly concern, regarding the collective dynamic behavior of fractional-order coupled systems.[35,36] Yu *et al.*[35] examined the complete synchronization and the SR phenomena of two coupled fractional harmonic oscillators, and reached the conclusion that the coupling strength and fractional order significantly impact the SR characteristics of OAG. Yan *et al.*[36] explored the particle synchronization and various types of SR mechanisms in a stochastic coupled system with fractional-order.

In summary, previous studies have primarily focused on fractional-order single-particle delay differential systems or fractional-order coupled systems without delays. Few researchers have comprehensively considered the combined effects of delay, fractional order, and coupling. Considering that fractional-order systems better describe dynamic systems with memory effects and non-local characteristics, and acknowledging the ubiquitous presence of potential-field delays and coupling delays in real-world systems, this paper investigates a fractional-order coupled stochastic dynamic system with both potential-field delay and coupling delay. Different from the model presented in Ref. [23], the model proposed in this paper incorporates the utilization of the Caputo fractional derivative operator. This operator serves to accurately depict the power-law memory characteristics exhibited by the system. Besides, the potential-field delay is used to characterize the time delay of Brownian motion in viscoelastic materials.[18] And the coupling delay is utilized to depict the transmission delay of coupling forces between particles.

The rest of the work is arranged as follows. Section 2 present the model description and preliminary results. In Section 3, several key theoretical results, encompassing the model's stability condition, the achievement of complete oscillator synchronization, and the derivation of the analytical expression for OAG, are obtained. In Section 4, the numerical simulation method and its effectiveness verification, and the accuracy analysis between two kinds of OAG through different methods are given. In Section 5, the collective dynamic behavior of the system, encompassing stability, synchronization, and resonance phenomena, are analyzed. Section 6 concludes some final remarks.

2. Model description and preliminaries

2.1. Model

The collective dynamical behavior of a globally coupled stochastic system with fractional-order and time delays is investigated in this paper. The specific expression of the model is described as

$$\begin{aligned}&\frac{\mathrm{d}^{\alpha}x_i(t)}{\mathrm{d}t^{\alpha}}+(\omega+\xi(t))x_i(t-\tau)\\&=\varepsilon\sum_{k=1}^{N}(x_k(t-\hat{\tau})-x_i(t-\hat{\tau}))+A_0\cos(\Omega t),\\&i=1,2,\ldots,N.\end{aligned}\tag{1}$$

Here, $x_i(t)$ denotes the displacement of the i-th particle at time t. A_0 and Ω represent the amplitude and frequency,

respectively, which are given by the external periodic force $A_0\cos(\Omega t)$.

The fractional order damping term is expressed as

$$\frac{\mathrm{d}^{\alpha}x_i(t)}{\mathrm{d}t^{\alpha}} = \int_0^t \frac{(t-\mu)^{-\alpha}}{\Gamma(1-\alpha)}\dot{x_i}(\mu)\,\mathrm{d}\mu, \tag{2}$$

where $0 < \alpha \leq 1$ and this equation defined as Caputo's fractional derivative operator. The convolution kernel, denoted as $h_{\mathcal{D}}(t)$, is given by $t^{-\alpha}/\Gamma(1-\alpha)$. This kernel signifies that the fractional-order damping term exhibits power-law memory, which corresponds to the memory properties observed in different viscoelastic materials and processes. When α equals 1, the fractional-order term reduces to an integer-order term.

In the term $(\omega+\xi(t))x_i(t-\tau)$ of the system, $\omega \geq 0$ signifies the intrinsic frequency and it can determine the size of the opening of a monostable potential field $U(x,t) = (w+\xi(t))x_i(t-\tau))/2$. The fluctuation of ω is described by the symmetric dichotomous noise $\xi(t)$, which refers to a type of noise that exhibits two distinct states with equal probabilities. On one side hand, the adoption of symmetric dichotomous noise makes the stochastic model easy to solve theoretically. One the other side, dichotomous noise approaches to Gaussian white noise and white granular noise in the limit, making it a prevalent choice across diverse physical and biological systems. The parameter $\tau > 0$ represents the time delay, acknowledging the fact that alterations in numerous dynamical systems are linked to their previous states. Specifically, τ in the model (1) denotes the propagation delay of the potential field force.

The term $\varepsilon\sum_{k=1,k\neq i}^{N}(x_k(t-\hat{\tau})-x_i(t-\hat{\tau}))$ represents the global coupling in the system. Here, $\varepsilon \geq 0$ represents the strength of the coupling, and N signifies the scale of the system. The global coupling arises from the direct connections between every particle in the system. Additionally, the transmission of coupling forces is accompanied by a time delay. To account for this delay, the delay $\hat{\tau} \geq 0$ is included in the coupling term.

2.2. Preliminaries

2.2.1. Symmetric dichotomous noise

The fluctuation of ω in Eq. (1) is given by symmetric dichotomous noise $\xi(t)$, which assumes two possible values $\{-\sigma,\sigma\}$ with corresponding probabilities

$$P_s(\sigma) = P_s(-\sigma) = \frac{1}{2}. \tag{3}$$

The mean of the random variable $\xi(t)$ and the correlation between $\xi(t)$ and $\xi(s)$ are given by

$$\langle\xi(t)\rangle = 0, \quad \langle\xi(t)\xi(s)\rangle = \sigma^2\,\mathrm{e}^{-\lambda|t-s|}. \tag{4}$$

The dichotomous process is a special case of a kangaroo process which satisfied the equation $\langle\xi(t)^4\rangle/\langle\xi(t)^2\rangle^2 = 1$. This is a type of colored noise with a simple property, causes extensive concern in physical process. The equation is solvable especially when dichotomous noise is applied to the fractional linear system.

Dichotomous noise is not only convenient for theoretical analysis in certain cases, but also have physical context and practical application. Dichotomous noise is a Markov process that first appeared in Morse code communication. Interference on the line can cause the telegraph signal to randomly switch between states, corresponding to this random process, which is also referred as random telegraph noise. Dichotomous noise can be described using a Bernoulli distribution, while Gaussian noise is described using a normal distribution. Under extreme conditions, dichotomous noise can be viewed as an extreme case of Gaussian noise. Dichotomous noise can arise from carious sources of noise, including thermal noise, mechanical vibrations, electronic noise, and more. It has a wide range of applications and phenomena that span multiple scientific and engineering fields such as communication, coding, signal processing, statistics, and network security.[37–39]

2.2.2. Fractional-order Shapiro–Loginov procedure

Suppose the variable $\xi(s)$ represents noise with exponential correlation, the functions $x_i(t)$ (where i ranges from 1 to N) depend on both time t and the process $\xi(s)$ for $0 < s \leq t$. By utilizing the renowned Shapiro–Loginov procedure,[40] the corresponding fractional-order differential equation can be readily derived as

$$\langle\xi(t)\frac{\mathrm{d}^{\alpha}x_i(t)}{\mathrm{d}t^{\alpha}}\rangle = \mathrm{e}^{-\lambda t}\frac{\mathrm{d}^{\alpha}}{\mathrm{d}t^{\alpha}}(\langle\xi(t)x_i(t)\rangle\,\mathrm{e}^{\lambda t}),$$
$$i = 1,2,\ldots,N. \tag{5}$$

2.2.3. Decoupling method for time delay

Considering $\xi(s)$ as an exponentially correlated noise, and $x(t)$ as a function of both t and $\xi(s)$ for $0 < s \leq t$, the authors in Ref. [23] provides a theoretical derivation yielding the following formula:

$$\langle\xi(t+\tau)x(t)\rangle = \mathrm{e}^{-\lambda\tau}\langle\xi(t)x(t)\rangle. \tag{6}$$

The formulas (5) and (6) mentioned above will play a key role in the later theoretical solution.

3. Theoretical results

3.1. Complete synchronization

In order to analyze the SR behavior in the system (1), it is necessary to determine whether the average behavior of the particles is synchronized first. To achieve this goal, we can calculate the average positional difference between particles, denoted as $\langle x_i(t)-x_j(t)\rangle, i \neq j$. To obtain this expression,

we can subtract the j-th equation from the ith equation in the model, resulting in the following description:

$$\begin{aligned}&\frac{\mathrm{d}^\alpha}{\mathrm{d}t^\alpha}(x_i(t)-x_j(t))+\omega(x_i(t-\tau)-x_j(t-\tau))\\&+(\xi(t)x_i(t-\tau)-\xi(t)x_j(t-\tau))\\&+\varepsilon(x_i(t-\hat{\tau})-x_j(t-\hat{\tau}))=0.\end{aligned}\tag{7}$$

By calculating the mean of Eq. (7), we obtain

$$\begin{aligned}&\frac{\mathrm{d}^\alpha}{\mathrm{d}t^\alpha}\langle x_i(t)-x_j(t)\rangle+\omega\langle x_i(t-\tau)-x_j(t-\tau)\rangle\\&+\langle\xi(t)x_i(t-\tau)-\xi(t)x_j(t-\tau)\rangle\\&+\varepsilon\langle(x_i(t-\hat{\tau})-x_j(t-\hat{\tau})\rangle=0.\end{aligned}\tag{8}$$

From Eq. (6), we have

$$\begin{aligned}&\langle\xi(t)x_i(t-\tau)-\xi(t)x_j(t-\tau)\rangle\\&=\mathrm{e}^{-\lambda\tau}\langle\xi(t-\tau)x_i(t-\tau)-\xi(t-\tau)x_j(t-\tau)\rangle.\end{aligned}\tag{9}$$

Denoting $z_1=\langle x_i(t)-x_j(t)\rangle$, $z_2=\langle\xi(t)x_i(t)-\xi(t)x_j(t)\rangle$, equation (8) can be rewrite as

$$\begin{aligned}&\frac{\mathrm{d}^\alpha}{\mathrm{d}t^\alpha}z_1(t)+\omega z_1(t-\tau)\\&+\varepsilon z_1(t-\hat{\tau})+\mathrm{e}^{-\lambda\tau}z_2(t-\tau)=0.\end{aligned}\tag{10}$$

There exist two independent variables, denoted as $z_1(t)$ and $z_2(t)$, in Eq. (10). To solve the variables, it is necessary to derive a new equation. Therefore, by multiplying Eq. (7) with $\xi(t)$, taking the average of the resulting equation, and applying the fractional-order Shapiro–Loginov formula (5), we obtain

$$\begin{aligned}&\mathrm{e}^{-\lambda t}\frac{\mathrm{d}^\alpha}{\mathrm{d}t^\alpha}(\langle\xi(t)x_i(t)-\xi(t)x_j(t)\rangle\mathrm{e}^{\lambda t})\\&+\omega\langle\xi(t)x_i(t-\tau)-\xi(t)x_j(t-\tau)\rangle\\&+\sigma^2\langle x_i(t-\tau)-x_j(t-\tau)\rangle\\&+\varepsilon\langle\xi(t)(x_i(t-\hat{\tau})-\xi(t)x_j(t-\hat{\tau})\rangle=0.\end{aligned}\tag{11}$$

Using decoupling formula (6) on Eq. (11), equation (11) can be rewrite as

$$\begin{aligned}&\mathrm{e}^{-\lambda t}\frac{\mathrm{d}^\alpha}{\mathrm{d}t^\alpha}(z_2(t)\mathrm{e}^{\lambda t})+\omega\mathrm{e}^{-\lambda\tau}z_2(t-\tau)\\&+\varepsilon\mathrm{e}^{-\lambda\hat{\tau}}z_2(t-\hat{\tau})+\sigma^2z_1(t-\tau)=0.\end{aligned}\tag{12}$$

Equations (10) and (12) are closed about $z_1(t)$ and $z_2(t)$. Applying Laplace transform method on Eqs. (10) and (12) we obtain

$$\begin{cases}a_{11}L(z_1)+a_{12}L(z_2)=a_{13},\\a_{21}L(z_1)+a_{22}L(z_2)=a_{23},\end{cases}\tag{13}$$

where $L(z_i)=\int_0^\infty\mathrm{e}^{-s\tau}z_i(t)\mathrm{d}t$, $i=1,2$, and

$$\begin{aligned}&a_{11}=s^\alpha+\omega\mathrm{e}^{-s\tau}+\varepsilon\mathrm{e}^{-s\hat{\tau}},\quad a_{12}=\mathrm{e}^{-(\lambda+s)\tau},\\&a_{13}=s^{\alpha-1}z_1(0),\quad a_{21}=\sigma^2\mathrm{e}^{-s\tau},\\&a_{22}=(s+\lambda)^\alpha+\omega\mathrm{e}^{-(\lambda+s)\tau}+\varepsilon\mathrm{e}^{-(s+\lambda)\hat{\tau}},\\&a_{23}=(s+\lambda)^{\alpha-1}z_2(0).\end{aligned}$$

Solving Eq. (13) we have

$$\begin{cases}L(z_1)=\dfrac{a_{13}a_{22}-a_{12}a_{23}}{a_{11}a_{22}-a_{12}a_{21}},\\[2ex]L(z_2)=\dfrac{a_{11}a_{23}-a_{21}a_{13}}{a_{11}a_{22}-a_{12}a_{21}}.\end{cases}\tag{14}$$

By employing the inverse Laplace transform to Eq. (14), the solution can be expressed as

$$z_i(t)=\sum_{k=1}^{2}h_{ik}(t)z_k(0),\quad i=1,2.\tag{15}$$

The relaxation functions $h_{ik}(t)$ are the inverse forms of the Laplace transforms $\hat{h}_{ik}(s)$ which can be given by Eq. (14). Referring to the findings in Ref. [41], we can ascertain the stability of the solution (15), implying that the solutions s_j of the equation

$$\begin{aligned}d(s)&=a_{11}a_{22}-a_{12}a_{21}\\&=(s^\alpha+\omega\mathrm{e}^{-s\tau}+\varepsilon\mathrm{e}^{-s\hat{\tau}})((s+\lambda)^\alpha+\omega\mathrm{e}^{-(\lambda+s)\tau}\\&\quad+\varepsilon\mathrm{e}^{-(s+\lambda)\hat{\tau}})-\sigma^2\mathrm{e}^{-(\lambda+2s)\tau}=0\end{aligned}\tag{16}$$

does not possess roots with a positive real part. This condition holds true when

$$\sigma^2<\sigma_{\mathrm{cr1}}^2=(\omega+\varepsilon)(\lambda^\alpha\mathrm{e}^{\lambda\tau}+\omega+\varepsilon\mathrm{e}^{\lambda(\tau-\hat{\tau})})\tag{17}$$

is fulfilled. Hence, we proceed with solving the synchronous system under the assumption that the inequality (17) holds. The functions $h_{ik}(t)$ tend to zero as time approaches infinity ($t\to\infty$) in the long-term regime, thereby diminishing the influence of initial conditions. Therefore, without any loss of generality, the initial conditions are considered as 0. By examining Eq. (14), we can deduce that $L(z_1)=L(z_2)=0$, indicating that $z_1=0$ and $z_2=0$. This can be rephrased as

$$\begin{aligned}&\langle x_i(t)\rangle=\langle x_j(t)\rangle,\langle\xi(t)x_i(t)\rangle=\langle\xi(t)x_j(t)\rangle,\\&i,j=1,2,\ldots,N.\end{aligned}\tag{18}$$

And due to the system's mean field being represented as

$$S(t)=\frac{1}{N}\sum_{i=1}^{N}x_i(t),\tag{19}$$

consequently, using Eq. (18), we can deduce

$$\langle S\rangle=\langle x_1\rangle=\langle x_2\rangle=\cdots=\langle x_N\rangle.\tag{20}$$

The examination of the mean field behavior plays a crucial role in the analysis of complex systems. Equation (20) demonstrating the statistical consistency between the behavior of individual particles and the mean field behavior, is utilized to achieve a specific analytical solution for the first moment $\langle x_i(t)\rangle$ and the corresponding OAG.

3.2. OAG of the model

The synchronization (20) is employed in the analysis of this section to achieve the specific analytical solution for $\langle x_i(t)\rangle$ and its corresponding OAG G. By directly averaging the model (1), we obtain

$$\frac{\mathrm{d}^\alpha}{\mathrm{d}t^\alpha}\langle x_i(t)\rangle + \omega\langle x_i(t-\tau)\rangle + \langle \xi(t)x_i(t-\tau)\rangle = A_0\cos(\Omega t). \quad (21)$$

In addition to $\langle x_i(t)\rangle$, equation (21) also includes another variable $\langle \xi(t)x_i(t-\tau)\rangle$. To solve the variables, it is necessary to create a new equation. Thus, by multiplying the ith equation with $\xi(t)$ in the model, averaging the gain equation, and applying the fractional-order Shapiro–Loginov formula, we obtain

$$\begin{aligned} &\mathrm{e}^{-\lambda t}\frac{\mathrm{d}^\alpha}{\mathrm{d}t^\alpha}(\langle \xi(t)x_i(t)\rangle \mathrm{e}^{\lambda t}) + \omega\langle \xi(t)x_i(t-\tau)\rangle \\ &+ \sigma^2\langle x_i(t-\tau)\rangle = 0. \end{aligned} \quad (22)$$

Denoting $y_1 = \langle x_i(t)\rangle$, $y_2 = \langle \xi(t)x_i(t)\rangle$, and using decoupling formula (6), equations (21) and (22) can be rewritten as

$$\begin{cases} \dfrac{\mathrm{d}^\alpha}{\mathrm{d}t^\alpha}y_1(t) + \omega y_1(t-\tau) + \mathrm{e}^{-\lambda\tau}y_2(t-\tau) = A_0\cos(\Omega t), \\ \mathrm{e}^{-\lambda t}\dfrac{\mathrm{d}^\alpha}{\mathrm{d}t^\alpha}(y_2(t)\mathrm{e}^{\lambda t}) + \omega\mathrm{e}^{-\lambda\tau}y_2(t-\tau) + \sigma^2 y_1(t-\tau) = 0. \end{cases} \quad (23)$$

Equation (23) is a closed equation set of $y_1(t)$ and $y_2(t)$. Applying Laplace transform on Eq. (23), we have

$$\begin{cases} b_{11}L(y_1) + b_{12}L(y_2) = A_0\dfrac{s}{s^2+\Omega^2} + b_{13}, \\ b_{21}L(y_1) + b_{22}L(y_2) = b_{23}, \end{cases} \quad (24)$$

where $L(y_i) = \int_0^\infty \mathrm{e}^{-s\tau}y_i(t)\,\mathrm{d}t$, $i = 1,2$, and

$$\begin{aligned} &b_{11} = s^\alpha + \omega\mathrm{e}^{-s\tau}, \quad b_{12} = \mathrm{e}^{-(\lambda+s)\tau}, \quad b_{13} = s^{\alpha-1}y_1(0) \\ &b_{21} = \sigma^2\mathrm{e}^{-s\tau}, \quad b_{22} = (s+\lambda)^\alpha + \omega\mathrm{e}^{-(\lambda+s)\tau}, \\ &b_{23} = (s+\lambda)^{\alpha-1}y_2(0). \end{aligned}$$

Solving Eq. (24) above we can get

$$\begin{cases} L(y_1) = \dfrac{b_{22}}{b_{11}b_{22}-b_{21}b_{12}}A_0\dfrac{s}{s^2+\Omega^2} + \dfrac{b_{13}b_{22}-b_{12}b_{23}}{b_{11}b_{22}-b_{12}b_{21}}, \\ L(y_2) = -\dfrac{b_{21}}{b_{11}b_{22}-b_{21}b_{12}}A_0\dfrac{s}{s^2+\Omega^2} + \dfrac{b_{11}b_{23}-b_{21}b_{13}}{b_{11}b_{22}-b_{12}b_{21}}. \end{cases} \quad (25)$$

By utilizing the inverse Laplace transform on Eq. (25), the solution can be expressed formally as

$$\begin{aligned} &y_i(t) = \sum_{k=1}^{2} H_{ik}(t)y_k(0) + A_0\int_0^t H_{i0}(t-t')\cos(\Omega t')\,\mathrm{d}t', \\ &i = 1,2. \end{aligned} \quad (26)$$

The relaxation functions $H_{ik}(t), k = 0,1,2$, represent the inverse Laplace transforms $\hat{H}_{ik}(s)$ determined by Eq. (25). In particular, $\hat{H}_{10}(s)$ serves as the transfer function of the system, denoted by the following specific expression:

$$\hat{H}_{10} = \frac{b_{22}}{b_{11}b_{22}-b_{21}b_{12}}.$$

Referring to the findings in Ref. [41], we can ascertain the stability of solution (26). This indicates that the solutions s_j of the equation

$$\begin{aligned} D(s) &= b_{11}b_{22} - b_{21}b_{12} \\ &= (s^\alpha + \omega\mathrm{e}^{-s\tau})((s+\lambda)^\alpha + \omega\mathrm{e}^{-(\lambda+s)\tau}) \\ &\quad - \sigma^2\mathrm{e}^{-(\lambda+2s)\tau} = 0 \end{aligned} \quad (27)$$

cannot possess roots with a positive real part. This condition holds true when

$$\sigma^2 < \sigma_{\mathrm{cr2}}^2 = \omega\lambda^\alpha\mathrm{e}^{\lambda\tau} + \omega^2 \quad (28)$$

is fulfilled. Therefore, we solve the system (23) under the premise that the inequality (28) is fulfilled. In the limit of infinite time ($t\to\infty$), the functions $H_{ik}(t)$ approach zero, and the effect of initial conditions becomes negligible. Hence, we make the assumption that the initial conditions are set to zero. Under this assumption, the mean particle displacement $y_1(t) = \langle x_i(t)\rangle$ is expressed as

$$\langle x_i(t)\rangle = A_0\int_0^t H_{10}(t-t')\cos(\Omega t')\,\mathrm{d}t'. \quad (29)$$

On the other side, the system (23) is also regarded as a linear time-invariant system. Based on response theory for such systems, the output signal follows a cosine waveform and differs from the input signal only in terms of amplitude and phase. Hence, the specific expression of $\langle x_i(t)\rangle$ is

$$\langle x_i(t)\rangle = A\cos(\Omega t + \varphi). \quad (30)$$

By performing the Laplace transform on Eq. (30) and comparing it with Eq. (29), A and φ can be obtained as

$$A = A_0|\hat{H}_{10}(\mathrm{j}\Omega)|, \quad \varphi = \arg(\hat{H}_{10}(\mathrm{j}\Omega)). \quad (31)$$

The specific functional expression of A and φ can be found in Appendix A. Besides, the specific expression for $\hat{H}_{10}(s)$ is

$$\hat{H}_{10}(s) = \frac{(s+\lambda)^\alpha + \omega\mathrm{e}^{-(\lambda+s)\tau}}{(s^\alpha + \omega\mathrm{e}^{-s\tau})((s+\lambda)^\alpha + \omega\mathrm{e}^{-(\lambda+s)\tau}) - \sigma^2\mathrm{e}^{-(\lambda+2s)\tau}}. \quad (32)$$

Finally, the OAG is obtained as

$$G = \frac{A}{A_0} = |\hat{H}_{10}(\mathrm{j}\Omega)|. \quad (33)$$

The inequality $\sigma_{\mathrm{cr1}}^2 > \sigma_{\mathrm{cr2}}^2$ can be easily proven, indicating that statistical synchronization must be exhibited when the system is stable. Consequently, throughout this document, we consistently assume that the noise amplitude σ adheres to the given inequality

$$\sigma^2 < \sigma_{\mathrm{cr2}}^2. \quad (34)$$

3.3. The small delay approximation of model (1)

Based on the small delay approximation method described in Ref. [42], we solve the model using the following theorem.

Theorem 1[42] Consider the following stochastic delay differential equation involving a state variable $x \in [a,b]$:

$$\mathrm{d}x(t) = f(x(t),x(t-\tau))\,\mathrm{d}t + \sigma g(x(t))\,\mathrm{d}W(t), \tag{35}$$

where the functions $f(x(t), x(t-\tau))$, and $g(x(t))$ are known, τ represents the time delay, and σ is a parameter that scales the intensity of the noise. The term $W(t)$ denotes a Wiener process, which starts at zero when $t=0$, and satisfies the conditions $\langle W(t)\rangle = 0$ and $\langle W^2(t)\rangle = t$. When the time delay τ is small, we can approximate $f(x(t),x(t-\tau))$ by performing a Taylor expansion around $x(t)$. This approximation leads to the following expression, obtained from the original stochastic delay differential Eq. (35):

$$\mathrm{d}x(t) = f_a(x(t))\,\mathrm{d}t + \sigma g_a(x(t))\,\mathrm{d}W(t), \tag{36}$$

where

$$f_a(x_0) \equiv f(x_0,x_0)\left[1-\tau\frac{\partial}{\partial x_\tau}f(x_0,x_0)\right],$$
$$g_a(x_0) \equiv g(x_0)\left[1-\tau\frac{\partial}{\partial x_\tau}g(x_0)\right],$$

the $x_0 \equiv x(t)$ and $x_\tau \equiv x(t-\tau)$ are used as dummy variables, and

$$\frac{\partial}{\partial x_\tau}f(x_0,x_0) \equiv \frac{\partial}{\partial x_\tau}f(x_0,x_\tau)|_{x_\tau=x_0}.$$

By utilizing Theorem 1, it is possible to derive the corresponding non-delay differential equation for Eq. (1)

$$\begin{aligned}&\frac{\mathrm{d}^\alpha x_i(t)}{\mathrm{d}t^\alpha} + \omega(1-\tau\omega)x_i(t) + (1-\tau)\xi(t)x_i(t)\\ &= \varepsilon\sum_{k=1}^{N}(x_k(t-\hat\tau)-x_i(t-\hat\tau)) + A_0\cos(\Omega t),\\ &\quad i=1,2,\ldots,N.\end{aligned} \tag{37}$$

By directly taking the average of Eq. (37), we obtain the following expression:

$$\begin{aligned}&\left(\frac{\mathrm{d}^\alpha}{\mathrm{d}t^\alpha}+\omega-\tau\omega^2\right)\langle x_i(t)\rangle + (1-\tau)\langle\xi(t)x_i(t)\rangle\\ &= A_0\cos(\Omega t).\end{aligned} \tag{38}$$

To solve this equation, we can multiply the i-th equation of the model by $\xi(t)$, average the resulting equation, and then apply the fractional-order Shapiro–Loginov formula (5):

$$\begin{aligned}&\mathrm{e}^{-\lambda t}\frac{\mathrm{d}^\alpha}{\mathrm{d}t^\alpha}(\langle\xi(t)x_i(t)\rangle\,\mathrm{e}^{\lambda t}) + (\omega-\tau\omega^2)\langle\xi(t)x_i(t)\rangle\\ &\quad+\sigma^2(1-\tau)\langle x_i(t)\rangle = 0.\end{aligned} \tag{39}$$

Equations (38) and (39) are closed for variables $X_1 = \langle x_i(t)\rangle$ and $X_2 = \langle\xi(t)x_i(t)\rangle$. By employing the same approach as described in Subsection 3.2, we can derive the following analytical expression:

$$X_1 = \bar{A}\sin(\Omega t+\phi). \tag{40}$$

Here, A represents the amplitude of X_1, while ϕ denotes its phase shift. The quantities A and ϕ can be denoted as

$$\bar{A} = A_0|\bar{H}(\mathrm{j}\Omega)|, \quad \phi = \arg(\bar{H}(\mathrm{j}\Omega)). \tag{41}$$

The function $\bar{H}(s)$ is given by

$$\bar{H}(s) = \frac{(s+\lambda)^\alpha+\omega-\tau\omega^2}{(s^\alpha+\omega-\tau\omega^2)((s+\lambda)^\alpha+\omega-\tau\omega^2)-\sigma^2(1-\tau)^2}. \tag{42}$$

Finally, the OAG can be determined as

$$\bar{G} = \frac{\bar{A}}{A_0} = |\bar{H}(\mathrm{j}\Omega)|. \tag{43}$$

4. Numerical simulation

In Subsection 4.1, a numerical simulation of the model (1) is conducted using power series expansion method. Building upon this numerical simulation algorithm, a comparative analysis of the accuracy of the theoretical results G and $\bar{G}$ is performed in Subsection 4.2.

4.1. Numerical simulation algorithm

When the time step $\Delta t = t_n - t_{n-1}$ is sufficiently small, the discrete-time approximation of model (1) can be represented by the following equation:

$$x_i(t_n) = -\sum_{m=1}^{n}(-1)^m\binom{\alpha}{m}x_i(t_{n-m}) + f_i(t_n)\Delta t^\alpha. \tag{44}$$

Here, the function $f_i(t_n)$ is denoted as

$$\begin{aligned}f_i(t_n) \;=\; &-(\omega+\xi(t_n))x_i(t_{n-1}-\tau) + \varepsilon\sum_{j=1}^{N}(x_j(t_{n-1}-\hat\tau)\\ &-x_i(t_{n-1}-\hat\tau) + A_0\cos(\Omega t_n),\end{aligned}$$

and $\xi(t_n)$ can be simulated by the method in Ref. [43].

Next, we evaluate the efficiency and accuracy of the numerical simulation algorithm by comparing the simulation result G_{num} with the theoretical result G. The simulation result G_{num} can be obtained from formula (44). Specifically in the simulation algorithm, we conduct K Monte Carlo experiments and use $x_i^k(t)$ to represent the k-th Monte Carlo experiment trajectory of the i-th particle. Thus, the estimated first moment of the displacement of the i-th particle is obtained as

$$\langle x_i(t)\rangle_{\mathrm{num}} = \frac{1}{K}\sum_{k=1}^{K}x_i^k(t). \tag{45}$$

According to formula (30), the first moment of a particle $\langle x_i(t)\rangle$ can be described as a cosine wave with the same frequency as the input signal $A_0\cos(\Omega t)$. Consequently, the

Fourier transform of $\langle x_i(t)\rangle_{\text{num}}$ can be used to simulate the amplitude of $\langle x_i(t)\rangle$, denoted as A_{num}. Therefore, the numerical simulation result G_{num} of the OAG G can be calculated by the formula $G_{\text{num}} = A_{\text{num}}/A_0$.

The accuracy of simulation algorithm is primarily influenced by the Monte Carlo experiment iterations K, simulation duration T, and time step Δt. Subsequently, the change curves of G_{num} with respect to these three variables are illustrated in Fig. 1. The trends depicted in Fig. 1 demonstrate that as K and T increase, and Δt decreases, G_{num} gradually converge towards G. By setting $\Delta t \le 0.005$, $K \ge 2000$, and $T \ge 120$, the relative error, denoted as $|(G_{\text{num}} - G)/G|$, remains below 10^{-2}. Hence, in this paper, we have employed fixed parameters for the numerical simulations: $\Delta t = 0.005$ (s), $K = 2000$, and $T = 120$ (s).

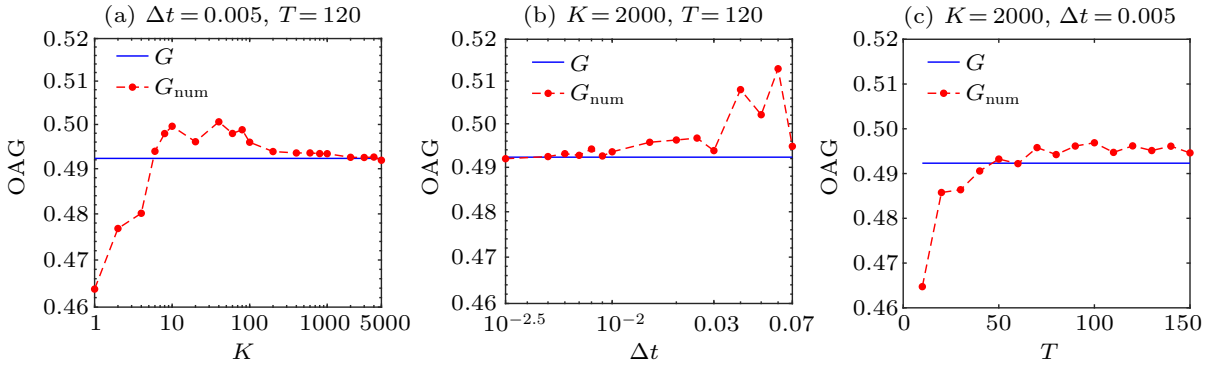


Fig. 1. Trajectory of G_{num} and G with $A_0 = 1$, $\Omega = 0.5\pi$, $\omega = 1$, $\lambda = 0.2$, $N = 6$, $\varepsilon = 1$, $\tau = 0.1$, $\hat{\tau} = 0.05$, $\sigma = 1$.

4.2. The accuracy analysis of theoretical results G and $\bar{G}$

The analytical expression Eq. (33) of OAG G by time delay decoupling formula is presented in Subsection 3.2. The analytical expression Eq. (43) of OAG $\bar{G}$ by small delay approximation is derived in Subsection 3.3. Thus, building upon the numerical simulation algorithm in Subsection 4.1, the accuracy analysis of these two theoretical results is given in this section.

From a theoretical perspective, delay decoupling method is a rigorous theoretical solving approach. So the error between G and the simulated G_{num} is independent of the potential field delay τ. On the other side, the small delay approximation theorem utilizes Taylor series expansion for approximate solving, resulting in an error between $\bar{G}$ and simulation G_{num} that increases with the increment of τ. To investigate the influence of τ on the accuracy of these two methods, we plot the variation curves of the absolute errors $\hat{G}_1 = G - G_{\text{num}}$ and $\hat{G}_2 = \bar{G} - G_{\text{num}}$ with respect to the delay τ, as shown in Fig. 2. From the two curves, we can clearly observe the following points.

(i) The absolute error of the time delay decoupling method (the curve $\hat{G}_1$) is solely influenced by the simulation, confirming its independence from the time delay τ.

(ii) The absolute error of the small delay approximation theorem (the curve $\hat{G}_2$) gradually increases with the increment of τ. This indicates that apart from the simulation error, the error is also influenced by time delay τ. The greater the delay, the larger the error.

(iii) When the time delay τ is small, both methods exhibit comparable solving accuracy. However, as τ increases, the advantages of the time delay decoupling method become more prominent.

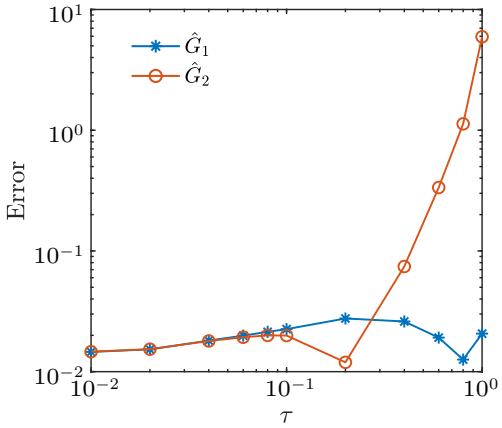


Fig. 2. Error between analytical results and simulation results with $A_0 = 1$, $\Omega = 0.5\pi$, $\omega = 1$, $\lambda = 0.2$, $\sigma = 0.5$, $\varepsilon = 1$, $N = 10$, $\hat{\tau} = 0.1$, $\Delta t = 0.005$ (s), $K = 2000$, $T = 120$ (s).

Based on the above analysis, we can conclude that the time delay decoupling method provides an accurate solution that is independent of the time delay and is an ideal solving approach. On the other hand, although the small delay approximation theorem exhibits high accuracy for small time delays, its error increases infinitely with the growth of the time delay, resulting in a significant decline in accuracy for large time delays. Hence, in the upcoming chapters, we will primarily study and analyze by using the theoretical solution G.

5. Collective behavior

In Subsection 5.1, we will examine the impact of the stability condition (28) on the behavior of N particles through the

numerical simulation algorithm. Subsection 5.2 validates the conclusion (20) through numerical simulation. And in Subsection 5.3, we explore the resonance behaviors of OAG G using the analytical expression derived from Eq. (33) in Appendix B.

5.1. Stability behavior

Building upon the stability condition Eq. (28), it is evident that when the inequality $\sigma^2 < \sigma_{\text{cr2}}^2$ is met, the system's output will remain within bounds as long as the input to the system is also within bounds. Therefore, this section examined the impact of the stability condition (28) on the behavior of N particles through the numerical simulation algorithm.

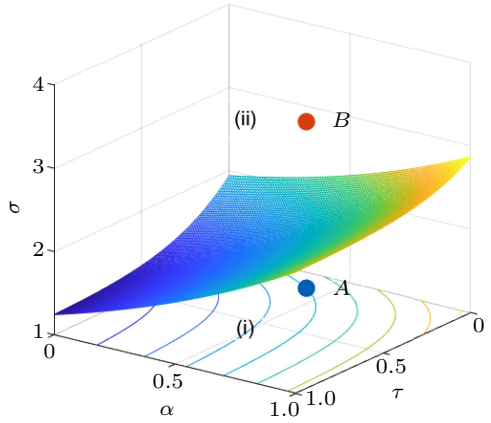


Fig. 3. Stability region of the system with $A_0 = 1$, $\Omega = 0.4\pi$, $\omega = 1.5$, $\lambda = 4$, $N = 6$, $\varepsilon = 1$ $\hat{\tau} = 0.05$.

According to the stability condition (28), we depict the image of stability region in the three-dimensional (3D) space (α, τ, σ) in Fig. 3. The 3D space can be partitioned into two distinct regions: region (i) represents the domain of stability, while region (ii) corresponds to the domain of the instability. The figure demonstrates that as α increases, the extent of the stability region (ii) expands, whereas it contracts with the increasing τ.

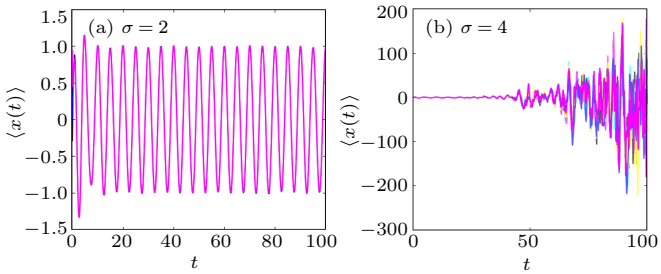


Fig. 4. Average particle displacement trajectory under $\alpha = 0.9$, $\tau = 0.8$, and different values of σ in panels (a) and (b).

In order to visually demonstrate the influence of system's stability condition, the average displacements of particles at point $A = (0.9, 0.8, 2)$ and point $B = (0.9, 0.8, 4)$, located within the stable region (i) and unstable region (ii) respectively in Fig. 3, were analyzed. And the corresponding curves are presented in Fig. 4. It is clearly observed in Fig. 4(a) that, the average displacements of particles remain within a finite range when the system fulfills the stability condition (28). Conversely, in Fig. 4(b), trajectories of average displacements diverge towards infinity when the system fails to satisfy the stability condition. These observations are consistent with the theoretical outcomes.

The study of collective dynamic behavior is meaningful only if the system is stable. Therefore, the simulations in the last two sections are conducted under the premise of ensuring Eq. (28) is met.

5.2. Synchronization behavior

The conclusion (20) is validated through numerical simulation in this section. According to Eq. (20), synchronization of N particles with distinct initial conditions occurs when the inequality $\sigma^2 < \sigma_{\text{cr2}}^2$ is satisfied.

Figure 5 gives information about the synchronization of the system. And the average displacement of N particles is shown in Fig. 5(a). To better represent the synchronization speed in a more intuitive manner, the variance $\Delta(t)$ of $\langle x_i(t)\rangle$ is given as

$$\Delta(t) = \frac{1}{N-1}\sum_{i=1}^{N}(\langle x_i(t)\rangle - \langle \bar{x}(t)\rangle)^2, \tag{46}$$

where the expression of $\langle \bar{x}(t)\rangle$ is

$$\langle \bar{x}(t)\rangle = \frac{1}{NK}\sum_{k=1}^{K}\sum_{i=1}^{N} x_i^k(t). \tag{47}$$

The curve of $\Delta(t)$ is plotted in Fig. 5(b).

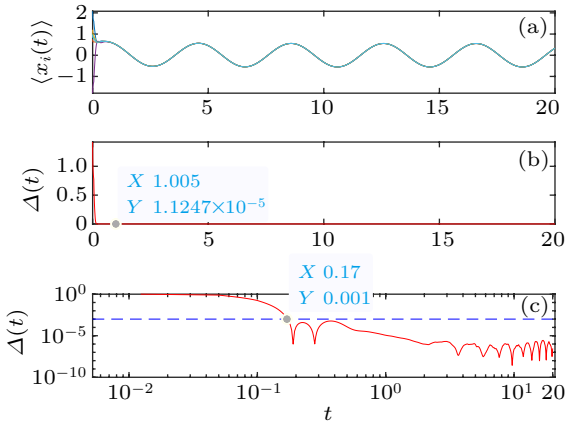


Fig. 5. Trajectories of N particles and the corresponding variance, including $A_0 = 1$, $\Omega = 0.5\pi$, $\omega = 1$, $N = 6$, $\lambda = 0.1$, $\sigma = 1$, $\alpha = 0.9$, $\varepsilon = 1$, $\tau = 0.1$, $\hat{\tau} = 0.05$.

In order to quantitatively analyze the time it takes for particles to synchronize, the concept of synchronization time is established as an indicator of the system's synchronization rate across various parameters. Since the number of simulation experiments are limited, the variance Δ may not diminish to zero over time. Hence, we make the assumption that the system

achieves synchronization when $\Delta \leq 10^{-3}$. Accordingly, the synchronization time t_0 is defined as

$$t_0 = \max\{t|\Delta(t) \geq 10^{-3}\}. \tag{48}$$

Figure 5(c) can be obtained by representing the variance curves' horizontal and vertical coordinates in logarithmic format in the second row.

By examining the initial row of subplots in Fig. 5, it becomes evident that regardless of the initial displacements of the particles, chosen uniformly, they will eventually attain a synchronized state after a certain duration of time. This observation is aligned to our previous theoretical analysis. It becomes apparent that the variance $\Delta(t)$ diminishes progressively over time and eventually falls below 10^{-3} in the second row of the figure. The third row of the figure reveals that, for the current parameter configuration, the synchronization time of the particles amounts to 0.17. In the subsequent phase, we will conduct a more detailed investigation into the synchronization of particles by exploring the influence of damping force and coupling force on the synchronization time t_0.

5.2.1. The effect of damping force

The presence of the fractional-order term (see Eq. (2)) in the system introduces damping force, which acts as a resistive force against particle motion. As the damping force increases, it becomes more effective in dissipating energy and reducing the oscillations in the system. This facilitates the particles' convergence towards a stable state by suppressing excessive movements and promoting smoother trajectories.

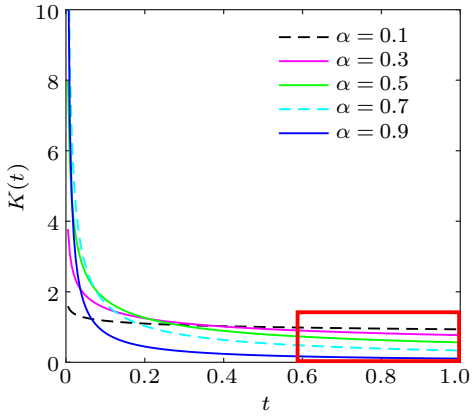


Fig. 6. Kernel damping functions under different orders.

The parameter α in the damping term affects the synchronization of the particles by changing damping force. It can be explained by Fig. 6. The power-law convolutional kernel, denoted as $K(t) = t^{-\alpha}/\Gamma(1-\alpha)$, in formula (2), introduces a long-term dependence on the historical velocity of particles in the damping term. Figure 6 shows the memory weight of the damping term curves for different α. In the region of larger time, $K(t)$ increases as α increases. Therefore, In this case, a smaller α corresponds to a stronger memory in the system, resulting in a greater damping force. A higher damping force leads to faster convergence of the N particle towards a stable state, facilitating synchronization among the particles. While, there is no such regularity in the region of smaller time of $K(t)$. As a result, when other parameters vary, changing the value of α can either increase or decrease the damping force.

In order to study the impact of α on the synchronization time t_0, the variation curves of t_0 with α taking in Fig. 7(a) is plotted, considering $\varepsilon = 0$ which implies the absence of coupling force among particles. Figure 7(a) demonstrates that as α increases, the synchronization time t_0 of the system also increases. This is because, in this scenario, the increase in α leads to a decrease in damping force, which slows down the system's convergence to a stable state and weaken its synchronization. Contrarily, figure 7(b) shows that t_0 decreases as α increases. This means under different other parameters, a higher value of α results in an enhanced damping force, which allows the system to reach a stable state more quickly, thereby reducing the synchronization time t_0.

Overall, fractional-order α affects the synchronization of the particles, and increasing α may either speed up or slow down the synchronization between particles.

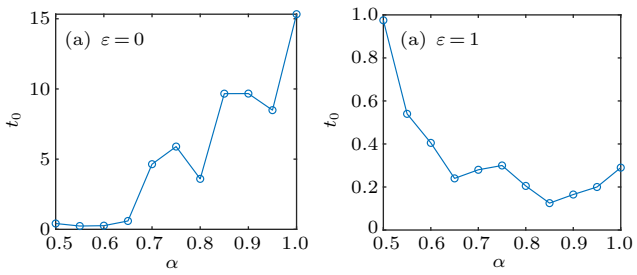


Fig. 7. Synchronization time t_0 to α under $A_0 = 1$, $\Omega = 0.5\pi$, $\omega = 1.5$, $\sigma = 1$, $N = 6$, $\lambda = 0.4$, $\tau = 0.1$, $\hat{\tau} = 0.05$, and different values of ε in panels (a) and (b).

5.2.2. The effect of coupling force

The impact of the coupling force and coupling parameters (ε and $\hat{\tau}$) on the synchronization of particles is given in this part. The presence of the coupling term

$$F_i(t) = \varepsilon \sum_{k=1}^{N} (x_k(t-\hat{\tau}) - x_i(t-\hat{\tau})) \tag{49}$$

in model (1) introduces coupling force. Since the coupling term only appears for $t > \hat{\tau}$, it is necessary to define an effective synchronization time t^* to characterize how ε and $\hat{\tau}$ impact synchronicity:

$$t^* = t_0 - \hat{\tau}. \tag{50}$$

Without loss of generality, the case is considered where $N = 2$ to examine the impact of coupling forces on synchronization. The coupling term can be interpreted as the presence of two additional forces

$$F_1(t-\hat{\tau}) = \varepsilon(x_2(t-\hat{\tau}) - x_1(t-\hat{\tau})),$$

$$F_2(t-\hat{\tau}) = \varepsilon(x_1(t-\hat{\tau}) - x_2(t-\hat{\tau})). \tag{51}$$

The F_1 and F_2 are two forces that have equal magnitudes but opposite directions. These forces will be exerted on the two particles at time t.

Figure 8 shows that, no matter what relative position relation between the two particles is, the particles move toward each other by setting $\hat{\tau} = 0$. In other words, the coupling forces cause the particles to be drawn towards one another at $\hat{\tau} = 0$. Thus, as coupling force increases, the attraction between the particles increases to make the system reach the synchronization faster, i.e., synchronization time t^* decreases.

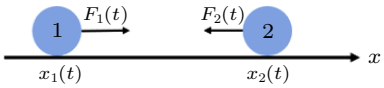


Fig. 8. The coupling forces between the two particles at time t by setting $\hat{\tau} = 0$.

As shown in Fig. 9, there are two kinds of relative position relations between the two particles because of random initial conditions and randomness introduced by noise in the motion of particles before the synchronization. Figure 9(a) reveals that, when the relative position of two particles at time t is the same as that at time $t-\hat{\tau}$, the coupling forces generated at time $t-\hat{\tau}$ cause the particles to attract each other at time t. While in Fig. 9(b), when the relative position of the two particles at time t is opposite as that at time $t-\hat{\tau}$, the coupling forces generated at time $t-\hat{\tau}$ make the particles repel each other at time t. In the process of particle motion, the attractive force will speed up the synchronization of the particles, while the repulsive force will prevent the particle from entering the synchronization state. Therefore, when the coupling delay $\hat{\tau}$ exists within the system, the effect of coupling forces on synchronization is nonlinear.

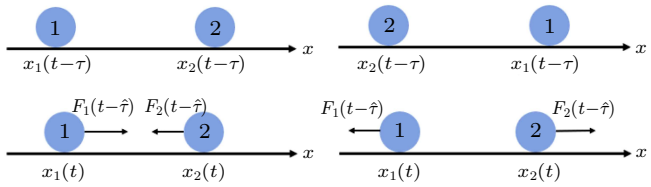


Fig. 9. The coupling forces between the two particles at time t by setting $\hat{\tau} > 0$: (a) the first kind of relative position, (b) the second kind of relative position.

According to the above analysis, the impact of coupling parameters on the synchronization time t^* is further studied through numerical simulation. Specifically, the synchronization of particles is influenced by altering the coupling force, which is contingent upon the coupling intensity ε and the coupling delay $\hat{\tau}$.

(i) Synchronization time t^* to ε

In Fig. 10(a), the relationship between the synchronization time t^* and the coupling intensity ε is plotted by setting $\hat{\tau} = 0$. The figure reveals that, as ε increases, the synchronization time t^* decreases, which means that the particles get into the synchronization state faster. And this phenomena can be explained by the Fig. 8.

In Fig. 10(b), the relationship between the synchronization time t^* and the coupling intensity ε is plotted by setting $\hat{\tau} = 0.05$. The figure shows a trend where the synchronization time t^* exhibits a decline followed by an incline as the parameter ε is augmented. For ease of narration, we use ε^* to represent the critical value, which implies that the $t^*(\varepsilon)$ exhibits a decreasing monotonicity when $\varepsilon \leq \varepsilon^*$, and an increasing monotonicity when $\varepsilon > \varepsilon^*$. With the current parameter settings in Fig. 10(b), the value of ε^* equals 0.9. The phenomenon in Fig. 10(b) can be explained by Fig. 9. When $\varepsilon \leq \varepsilon^*$, the attraction between particles dominates. Therefore, as the value of ε increases, the coupling force increases, the attraction between particles increases to speed up the synchronization. Thus, as ε increases to ε^*, the value of t^* decreases. When $\varepsilon > \varepsilon^*$, the repulsion between particles dominates. Therefore, as the value of ε increases, the coupling force increases, the repulsion between particles increases to prevent the particle from entering the synchronization state. Thus, as the value of ε increases, the value of t^* also increases.

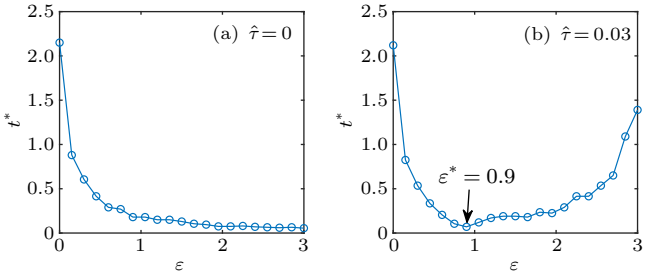


Fig. 10. The synchronization time t^* to ε under $A_0 = 1$, $\Omega = 0.5\pi$, $\omega = 2$, $\sigma = 1.5$, $\lambda = 2$, $N = 10$, $\alpha = 0.9$, $\tau = 0.05$, and different values of $\hat{\tau}$ in panels (a) and (b).

(ii) Synchronization time t^* to $\hat{\tau}$

To explain the phenomena in Fig. 11, we first give the inequality that the coupling force F_1 satisfies

$$F_1(t-\hat{\tau}_1) > F_1(t-\hat{\tau}_2), \tag{52}$$

where $\hat{\tau}_1 > \hat{\tau}_2$. This is because, regardless of the relative position of the particles in Fig. 9, the distance between the particles will become smaller and smaller until they are synchronized. Then we can conclude that the coupling force between particles increases as the coupling delay $\hat{\tau}$ increases.

Without loss of generality, to illustrate the relationship between t^* and $\hat{\tau}$ is plotted by setting $\varepsilon = 0.2$ in Fig. 11(a), and $\varepsilon = 1$ in Fig. 11(b). Since the other parameters in this figure are set as the same as in Fig. 10, the ε^* mentioned in the following is the same as in Fig. 10(b), which means $\varepsilon^* = 0.9$.

In Fig. 11(a), since $\varepsilon < \varepsilon^*$, the attraction between particles dominates. The figure shows that the value of t^* decreases

as $\hat{\tau}$ increases. This indicates that an increase in $\hat{\tau}$ significantly accelerates the synchronization speed of particles. We use Eq. (52) to explain the phenomena. As the value of $\hat{\tau}$ increases, the coupling force increases, leading to a greater attraction between particles. Consequently, particles can enter synchronization state faster as $\hat{\tau}$ increases, leading to decrease of t^*.

In Fig. 11(b), the relationship between t^* and $\hat{\tau}$ is plotted by setting $\varepsilon = 1$. Since $\varepsilon > \varepsilon^*$, the repulsion between particles dominates. As $\hat{\tau}$ increases, the coupling force increases, the repulsion between the particles is enhanced, making the system enter the synchronization state more slowly. Therefore, the value of t^* increases as the value of $\hat{\tau}$ increases in Fig. 11(b).

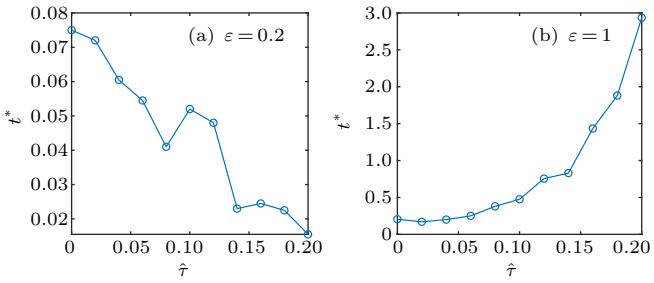


Fig. 11. Synchronization time t^* to $\hat{\tau}$ under $A_0 = 1$, $\Omega = 0.5\pi$, $\omega = 2$, $\sigma = 1.5$, $\lambda = 2$, $N = 10$, $\alpha = 0.9$, $\tau = 0.05$, and different values of ε in panels (a) and (b).

5.3. Resonance behavior

This section explores the resonance behaviors of OAG G using the analytical expression derived from Eq. (33) in Appendix B. the focus of this section is on the impact of the fractional-order term, the potential field term, and the coupling term on the system's resonance behavior. The fractional-order term is influenced by the fractional order α. The potential field term is affected by the noise intensity σ and the potential field delay τ. When τ matches the driving force Ω, it can lead to the phenomenon of periodic resonance. The coupling term is influenced by the coupling strength ε, coupling delay $\hat{\tau}$, and system size N. However, we have previously concluded in the literature that ε and N have similar effects on synchronization. Therefore, to highlight the key points and ensure the integrity of the structure, this paper mainly discusses the effects of the parameters α, σ, τ, Ω, ε, and $\hat{\tau}$ on the system's resonance behavior.

5.3.1. Stochastic resonance behavior

The phenomenon of SR aries from the optimal match achieved through the competition between order and randomness under nonlinear conditions. The randomness is introduced by multiplicative noise $\xi(t)$. As the value of σ increases, the random force is strengthened, leading to a higher degree of randomness in the system.

The order is provided by ordered force which is composed by viscous damping force $\mathrm{d}^\alpha x_i(t)/\mathrm{d}t^\alpha = \int_0^t (t-\mu)^{-\alpha}/\Gamma(1-\alpha)\dot{x}_i(\mu)\mathrm{d}\mu$, potential field force $\partial U(x,t)/\partial x = (\omega - \xi(t))x(t-\tau)$ and driving force $A_0\cos(\Omega t)$. Correspondingly, the damping force is influenced by α, the potential field is influenced by ω and τ, and the driving force is influenced by its amplitude A_0 and frequency Ω. With the alteration of the aforementioned parameters, the ordered force and random force of the system undergo changes, leading to a competition between orderliness and randomness. When orderliness and randomness reach an optimal match, SR occurs. Since the influence of ω and A_0 on the ordered force is linear, extensive research has already been conducted in numerous studies. Therefore, we will not discuss the impact of these two parameters in this paper. Due to the nonlinear nature of the variation of damping force with respect to α, as well as the nonlinear variations of the potential field force with respect to τ and Ω, the specific correlations and their dependence on the remaining parameters are context-specific.

(i) Conventional stochastic resonance

This examined the SR phenomenon in relation to the noise amplitude σ, guided by the aforementioned SR mechanism. This phenomenon is commonly referred to as conventional stochastic resonance (CSR), which refers to the non-monotonic relationship between G and σ.

To analyze the CSR phenomenon of $G(\sigma)$, the phase diagram of the α–τ plane is presented in Fig. 12. It is shown that the resonance region gradually becomes narrower as τ increases. That is, CSR phenomena disappears in the region where α is small and τ is relative large. We employ the SR mechanism to explain this phenomenon. Under the current parameter settings, with decreasing α, the convolution kernel increases, the damping term possesses a better memory, leading to enhance the damping force. Therefore, in the region where the value of α is small, the damping force provides the system with a stronger sense of order, effectively constraining the system's randomness to a lower level. Besides, as τ increases, potential field term $\partial U(x,t)/\partial x$ increases, resulting in more order for the system. Thus, both small α and large τ are contribute to a high degree of order in this region. Hence, the order is too much to compete with the limited randomness which is provided by $\sigma < \sigma_{\mathrm{cr2}}$.

In Fig. 13, the relationship between G and σ is explored while considering different values of α and τ. To simplify the analysis,we focus on the impact of α and τ on σ-induced CSR by setting $\tau = 1$ in Fig. 13(a), and $\alpha = 0.9$ in Fig. 13(b). Curves in Fig. 13 demonstrate a remarkable phenomenon of single-peak resonance when α and τ fall within the resonance region in Fig. 12.

Figure 13(a) shows that as α increases, the maximum value of $G(\sigma)$ rises and the resonant peak shifts towards the left. Here, the larger α means more order, needs more randomness to offer more randomness, i.e., larger σ, to achieve

optimal matching for CSR, obeying the analysis in the phase diagram Fig. 12 that increasing α decreases the system's order.

Figure 13(b) shows that with increasing τ, the maximum value of $G(\sigma)$ decreases, and the resonance peak shifts towards the right. This observation aligns with the findings presented in Fig. 12, where an increasing τ leads to an amplified potential field that enhances system organization. Consequently, a higher degree of randomness is required to achieve the optimal match. Consequently, the peak of $G(\sigma)$ progressively shifts towards higher values of σ as τ increases.

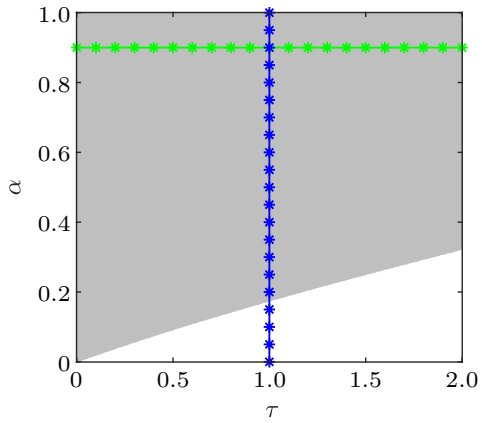


Fig. 12. Phase diagram of $G(\sigma)$ for CSR in α–τ plane, including $\omega = 1.5$, $\Omega = 0.05\pi$, $\lambda = 0.5$. The absence of CSR is represented by the white region, while the presence of single-peak resonance is indicated by the gray region.

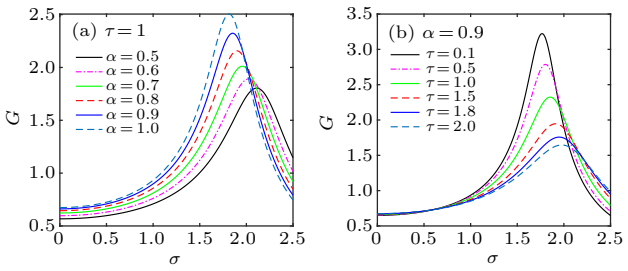


Fig. 13. CSR of $G(\alpha)$ with different values of α in panel (a) and different values of τ in panel (b).

(ii) General stochastic resonance

Under the guidance of the aforementioned SR mechanism, the influence of Ω and τ is investigated on the system in this section. This phenomenon corresponds to a phenomenon known as generalized stochastic resonance (GSR), which is commonly referred to as SR in a broader context. GSR encompasses the existence of a non-monotonic relationship between specific functions of the output signal (such as moments, autocorrelation, and signal-to-noise ratio) and the parameters of system.

(I) GSR phenomenon of $G(\Omega)$

In Fig. 14, the phase diagram of α–σ plane is plotted by setting $\tau = 0.1$ to analyze the GSR phenomenon of $G(\Omega)$. The figure shows that GSR occurs in relative high noise amplitude region. This implies a sufficiently strong noise is required to provide randomness to induce GSR with respect to Ω.

Without loss of generality, the curves of $G(\Omega)$ are plotted under different values of σ and α respectively by setting $\alpha = 0.5$ in Fig. 15(a), and $\sigma = 2$ in Fig. 15(b). As shown in Fig. 15 that when both σ and α fall within the resonance region of Fig. 14, $G(\Omega)$ curves display single-peak resonance phenomenon.

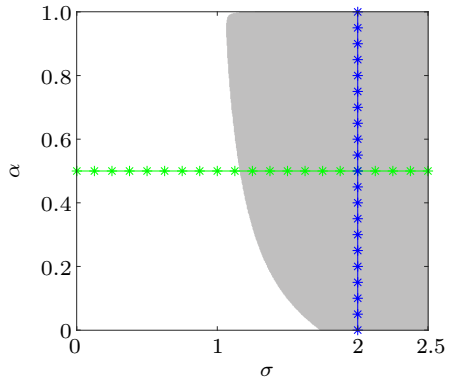


Fig. 14. Phase diagram of $G(\Omega)$ for GSR in α–σ plane, including $\omega = 1$, $\tau = 0.1$, $\lambda = 0.2$. The absence of GSR is represented by the white region, while the presence of single-peak resonance is indicated by the gray region.

Figure 15(a) reveals that as σ increases, the peak of $G(\Omega)$ decreases, and the peak position shifts towards larger values of Ω. It can be concluded that the increased randomness of the system under fixed order conditions needs large value of Ω to ensure maximum the value of G. This implies under the current parameter settings, increasing Ω enhances the external driving force, thereby increasing the system's level of order. In Fig. 15(b), as α increases gradually, the peak position of $G(\Omega)$ moves to the left and its value decreases. This is because under the current parameter settings, increasing α increases the damping force, leading to reduction of the randomness of the system, and it requires an increase in Ω to ensure the occurrence of SR. This is consistent with the non-monotonic property of the effect of α on damping force.

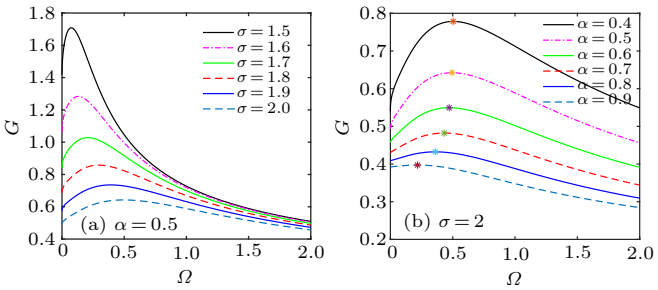


Fig. 15. GSR phenomenon of $G(\Omega)$ with different values of σ in panel (a) and different values of α in panel (b).

(II) GSR phenomenon of $G(\tau)$

In Fig. 16, the phase diagrams of the α–σ plane is presented to analyze GSR phenomenon for $G(\tau)$. The figure indicates that GSR is absent in the low noise amplitude region. Under the conditions of order provided by the potential field force, damping force, and driving force, a small value of σ

fails to provide sufficient randomness to match the order of the system, resulting in the absence of GSR. Besides, as α decreases, the resonance region gradually narrows. This phenomenon is attributed to the fact that, under the current parameter settings, smaller values of α contribute greater damping force to the system. Consequently, in the region where α is small, larger damping forces provide more order to the system. Hence, more randomness from noise is required to ensure that $G(\Omega)$ exhibits GSR phenomenon.

Without loss of generality, GSR phenomenon of $G(\tau)$ with different α and σ is examined by setting $\sigma = 2$ and $\alpha = 0.9$ in Figs. 17(a) and 17(b). Figure 17 demonstrates that when α and σ fall within the resonance region illustrated in Fig. 16, $G(\tau)$ curves show the occurrence of a single-peak resonance phenomenon.

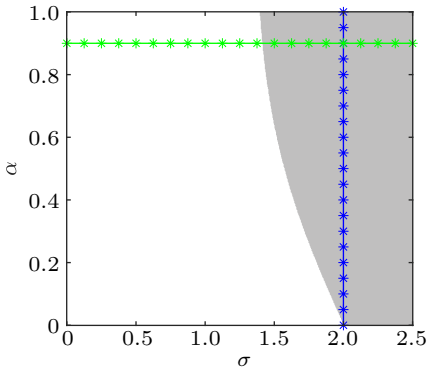


Fig. 16. Phase diagram of $G(\tau)$ for GSR in α–σ plane with $\omega = 1$, $\Omega = 0.1$, $\lambda = 0.9$. The absence of GSR is represented by the white region, while the presence of single-peak resonance is indicated by the gray region.

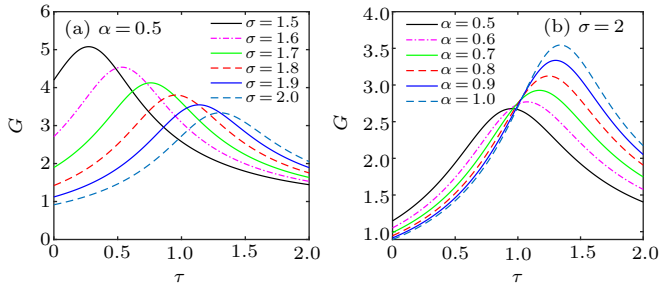


Fig. 17. GSR phenomenon of $G(\tau)$ with different values of σ in panel (a) and different values of α in panel (b).

Figure 17(a) shows that with an increase in σ, there is a shift of the resonant peak towards the right and a reduction in the peak value of $G(\tau)$. Increasing σ introduces more randomness for the system, needing more order to obtain the optimal matching. In this case, the value of τ increases to provide more potential field force, i.e. more order. This is attributed to the fact that, under the current parameter settings, larger values of τ contribute greater potential field force to the system. Therefore, the peak of $G(\tau)$ experiences a rightward shift as σ increases. The observation depicted in Fig. 17(b) reveals that as α rises, the peak of $G(\tau)$ increases and the resonant peak undergoes a rightward displacement. This is because under the fixed randomness, increasing τ enhances the system's order, thereby offsetting the decay in order caused by increasing α.

5.3.2. Periodic resonance behavior

Periodic resonance (PR) phenomenon arises when there exists a periodic matching between the external driving frequency Ω and the potential field delay τ. In this section, we will discuss the PR mechanism and PR phenomena. To elucidate the PR mechanism, we first analyze the variations of the OAG G in relation to both Ω and τ in the absence of noise. Building upon this analysis, when the system is subjected to noise, we further investigate the occurrence of superposition resonance phenomena which is combined with the PR and the previously discussed SR.

In Appendix B, we get the theoretical expression of OAG

$$G_{\mathrm{r}} = \frac{1}{\sqrt{\Omega^{2\alpha} + \omega^2 + 2\omega\Omega^{\alpha}\cos(\Omega\tau + \pi\alpha/2)}} \tag{53}$$

without noise. According to the expression of G_{r}, we can conclude that when

$$\Omega\tau + \frac{\pi}{2}\alpha = \pi + 2k\pi, \quad k = 0, \pm 1, \pm 2, \ldots \tag{54}$$

satisfied, G_{r} gets the maximum value. This means as $\Omega(\tau, \alpha)$ changes, $G_{\mathrm{r}}(\Omega)$, $(G_{\mathrm{r}}(\tau), G_{\mathrm{r}}(\alpha))$ will periodically reach its maximum value.

Since α is constrained to the interval $(0, 1]$, $G_{\mathrm{r}}(\alpha)$ does not possess periodic properties. Therefore, we will now discuss the periodic properties of $G_{\mathrm{r}}(\Omega)$ and $G_{\mathrm{r}}(\tau)$, with their corresponding phases being $\pi\alpha/2$. It is worth noting that, $G_{\mathrm{r}}(\tau)$ is a strict periodic function with a period of $2\pi/\Omega$, and the phase of its denominator is $\pi\alpha/2$. While $G_{\mathrm{r}}(\Omega)$ is a quasi-periodic function, which implies although $G_{\mathrm{r}}(\Omega) = G_{\mathrm{r}}(\Omega + T)$ is not satisfied, as Ω increases, $G_{\mathrm{r}}(\Omega)$ periodically reaches local maximum values with a period of $2\pi/\tau$ approximately. In summary, we can conclude that without noise, PR phenomena occur when Ω and τ match periodically.

When system is affected by noise, the occurrence of resonance phenomenon under the combined influence of the SR and PR mechanisms is explored. On the one side, the periodic matching between Ω and τ will not disappear, ensuring the persistence of PR phenomenon. On the other side, the presence of noise introduces the randomness for the system, leading to the optimal matching with order. Thus, both SR and PR phenomena happen, leading to a superposition resonance.

According to the above analysis, we validate the theoretical solution of the model with simulation by setting $\sigma = 0$ in item (i) of Subsubsection 5.3.2. And in item (ii) fo Subsubsection 5.3.2, we use PR mechanism and SR mechanism to explain the periodic resonance and multi-peaks resonance shown.

(I) PR without noise

Based on the PR mechanism, the resonance behavior of OAG $G_{\rm r}$ with respect to Ω and τ is analyzed by setting $\sigma = 0$ in this section.

(I) PR phenomenon of $G_{\rm r}(\tau)$

In Fig. 18, the phase diagram of $G_{\rm r}(\tau)$ is plotted for PR phenomenon in Ω–α plane to verify the PR mechanism without noise. The figure shows that as Ω increases, the PR occurs, accompanied by a corresponding rise in the quantity of resonance peaks. This demonstrates the periodic properties of $G_{\rm r}(\tau)$. Further more, the boundaries of the resonance region are parallel and slanting towards the lower right direction as α increases. This demonstrates the shifting property of α.

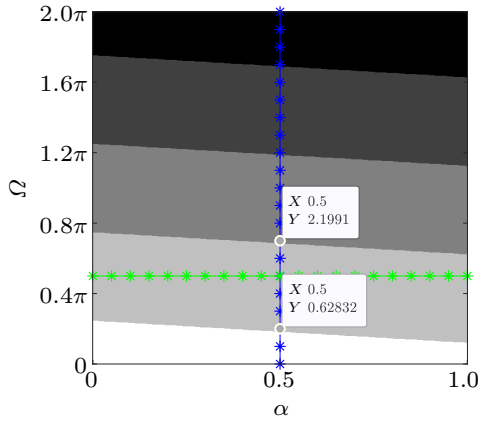


Fig. 18. Phase diagram illustrating the behavior of $G_{\rm r}(\tau)$ for PR in the α–τ plane, including $\omega = 1.5$, $\sigma = 0$, $\lambda = 0$. The absence of PR is depicted by the white region, and with the deepening of gray color, the number of resonant-peak gradually increases from 1 to 4.

In order to quantitatively describe the theory of PR, the effect of Ω and α on τ-induced PR is analyzed. In Fig. 19(a), the curves of $G_{\rm r}(\tau)$ with different values of Ω are plotted by fixing $\alpha = 0.5$. The figure shows that the curves $G_{\rm r}(\tau)$ exhibit no resonance, single-peak resonance, and multi-peaks resonance when the value of Ω falls within the corresponding resonance region. Moreover, according to the relation (54), the spacing between the peaks of each resonance curve $G_{\rm r}(\tau)$ in the graph strictly satisfies the minimal positive period of $G_{\rm r}(\tau)$: $2\pi/\Omega$. For example, the spacing between resonance peaks is 2 by setting $\Omega = \pi$.

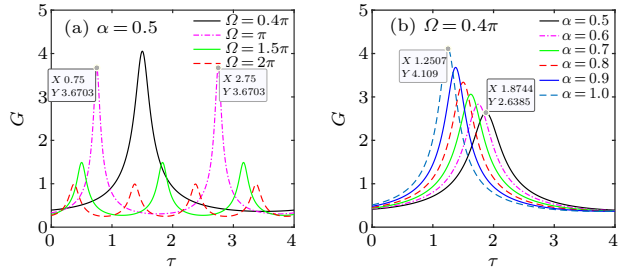


Fig. 19. The PR phenomenon of $G_{\rm r}(\tau)$ with different values of Ω in panel (a) and different values of α in panel (b).

In Fig. 19(b), $G(\tau)$ curves with different α is presented by setting $\Omega = 0.5\pi$. According to the relation (54), the distance between the resonance peak of the two curves with α_1 and α_2 is $|(\alpha_1 - \alpha_2)\pi/2\Omega|$. For example, the distance between the curve $\alpha = 0.5$ and the curve $\alpha = 1$ is 0.625.

(II) PR phenomenon of $G_{\rm r}(\Omega)$

In Fig. 20, the phase diagram of $G_{\rm r}(\Omega)$ is plotted for PR in τ–α plane to verify the PR mechanism without noise. The figure shows the similar periodic phenomenon observed in Fig. 18, demonstrates the quasi-periodic properties of the curves $G_{\rm r}(\Omega)$.

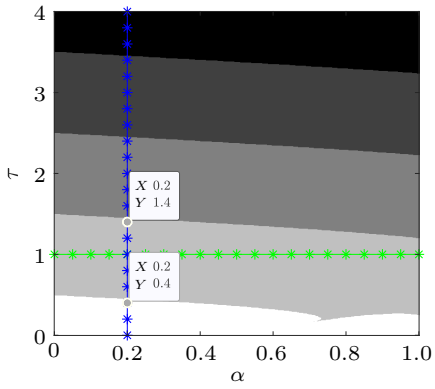


Fig. 20. Phase diagram of $G_{\rm r}(\Omega)$ for PR in α–τ plane, including $\omega = 2, \sigma = 0, \lambda = 0$. The absence of PR is depicted by the white region, and with the deepening of gray color, the number of resonant-peak gradually increases from 1 to 4.

Without loss of general, in order to quantitatively describe the influence of τ and α on Ω-induced PR, the curves $G_{\rm r}(\Omega)$ are presented by fixing $\alpha = 0.2$ in Fig. 21(a), and $\tau = 1$ in Fig. 21(b). From the numerical values in the graph, it can be observed that the curves $G_{\rm r}(\Omega)$ satisfy Eq. (54) approximately, no longer strictly.

Figure 21(a) shows that the curves $G_{\rm r}(\Omega)$ exhibit no resonance, single-peak resonance, and multi-peaks resonance when the value of τ falls within the corresponding resonance region in Fig. 20. Moreover, the spacing between the peaks of each resonance curve $G_{\rm r}(\Omega)$ in the graph satisfies the formula approximately: $2\pi/\tau$. For instance, by setting $\tau = 4$, the spacing between resonance peaks is approximately 0.5π.

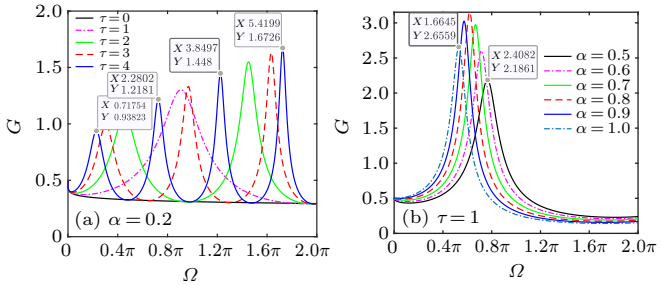


Fig. 21. The PR phenomenon of $G_{\rm r}(\Omega)$ with different values of τ in panel (a) and different values of α in panel (b).

In Fig. 21(b), the curves of $G_{\rm r}(\Omega)$ with different α are presented by fixing $\tau = 1$. According to the relation (54), the distance between the resonance peaks of the two curves with α_1 and α_2 approximately satisfies the formula: $|(\alpha_1 - \alpha_2)\pi/2\tau|$. For example, the distance between the curve $\alpha = 0.5$ and the curve $\alpha = 1$ is approximately equal to 2.

(ii) PR with noise

In this section, we delve into the manifestation of resonance phenomenon when both the SR and PR mechanisms exert their combined influence.

(I) PR phenomenon of $G(\tau)$

In Fig. 22, the phase diagram of the Ω–σ plane is plotted to analyze the resonance phenomenon for $G(\tau)$. The phase diagram exhibits a similar periodicity to Fig. 18, showing an increase in the number of resonance peaks as Ω increases with a periodic pattern. Furthermore, within the region (i) depicted in Fig. 22, it can be observed that an extra resonance peak overlaps with the existing periodic resonance peaks. This is because the resonant peaks of $G(\tau)$ in region (i) are composed of both PR and GSR.

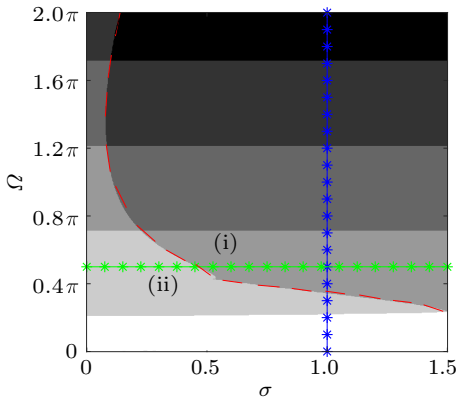


Fig. 22. Phase diagram of $G(\tau)$ in the Ω–σ plane, including $\omega = 2, \alpha = 0.3, \lambda = 0.5$. The absence of PR is depicted by the white region, and with the deepening of gray color, the number of resonant-peak gradually increases from 1 to 5.

Without loss of generality, the resonance phenomenon of $G(\tau)$ with different Ω and σ is analyzed, by setting $\sigma = 1$ and $\Omega = 0.5\pi$ in Figs. 23(a) and 23(b). Figure 23 shows that when both Ω and σ fall within the resonance region depicted in Fig. 22, the $G(\tau)$ curves show various resonance phenomena, including single-peak, double-peak, and multi-peak resonances.

Figure 23(a) shows that the curves $G(\tau)$ exhibit two kinds of peak resonances when the values of Ω fall within the corresponding resonance region (i) of Fig. 22. The occurrence of periodic resonance peaks can be marked with the symbol '$*$', which fails to satisfy Eq. (54) strictly. This implies that the presence of the noise causes a displacement of the resonance peak positions in Fig. 19, and the magnitude of this displacement is controlled by the noise amplitude σ. For example, on the curve with $\Omega = \pi$, the position of the resonance peak at $\tau = 1.05$ fails to satisfy $\tau = (\pi - 0.5\alpha\pi)/\Omega = 0.85$ strictly, and the displacement is 0.2. Moreover, the spacing between the second and third resonance peaks is 1.8, which differs from the theoretical result $2\pi/\Omega = 2$ by approximately 0.2. It is worth to mention that, the resonance also occurs in the low τ region, which is different from Fig. 19. We mark this kind of resonance peaks as '$\circ$', which appears before periodic resonance peaks. And these resonance peaks are similar to Fig. 17.

In Fig. 23(b), $G(\tau)$ curves with different values of σ are plotted while keeping $\Omega = 0.5\pi$ constant. Figure 23(b) demonstrates that when $\sigma = 0$, the $G(\tau)$ curve exhibits single-peak resonance. This corresponds to the PR phenomenon discussed in Fig. 19. As the value of σ increases, the curves gradually transition into double-peak resonances, which is the result of the superposition of PR resonance and SR resonance. Additionally, the positions of the resonance peaks shift as σ changes. This is because the change in σ introduces randomness in the system, requiring a corresponding adjustment in τ to maintain the proper balance between order and randomness.

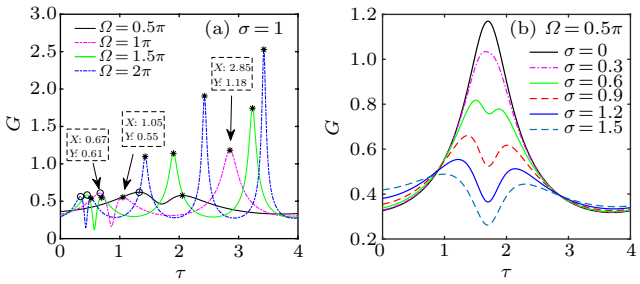


Fig. 23. PR phenomenon of $G(\tau)$ with different values of Ω in panel (a) and different values of σ in panels (b).

(II) PR phenomenon of $G(\Omega)$

Similarly to $G(\tau)$, the resonance phenomenon of $G(\Omega)$ exhibits a similar periodicity and superposition effect as discussed in the first part. Therefore, this phenomenon will not be repeated in further discussion in this part.

To further analyze the superposition effect of PR mechanism and SR mechanism, we plot the curves $G(\Omega)$ with different σ by setting τ. Figure 24(a) shows that there is a noticeable distance between the PR resonance peaks and the GSR resonance peaks. Similar to Fig. 15, the first peak of $G(\Omega)$ is the result of optimal matching between randomness and order, obeying the SR mechanism. The second and third peaks of $G(\Omega)$ are the result of periodic matching between Ω and τ.

Figure 24(b) shows that the curve $G(\Omega)$ exhibits single-peak by setting $\sigma = 0$. This is the PR phenomenon which has been discussed in Fig. 21. As σ increases, the SR appears, and the curves gradually show double-peak resonance. In addition, the close proximity of the two resonance peaks makes it difficult to distinguish their individual properties numerically. This is a superposition effect of resonance peaks resulting from the interaction of the two resonance mechanisms. It is worth mentioning that under the parameter settings in Fig. 24(a), it is easy to distinguish between the two resonance peaks. However, under the parameter settings in Fig. 24(b), we can qualitatively observe the occurrence of both types of resonance, but it is not possible to numerically distinguish between these two categories of resonance peaks.

In stochastic dynamical systems, time delay typically exist in the potential field terms. In bistable systems, potential field delay can alter the height and width of the potential barrier, thereby affecting the transition probability of particles between the two equilibrium points. As a result, weak periodic signals can be enhanced under appropriate potential field delay. In our system, when the potential field delay matches the driving frequency, the output of the system can be enhanced periodically, making the system's response more pronounced. Therefore, in the application, by adjusting the potential field delay, the system's response to weak periodic signals can be enhanced, leading to better prediction and control of complex system behaviors. This can be applied in the field of weak signal detection, which means a new methods of signal detections.

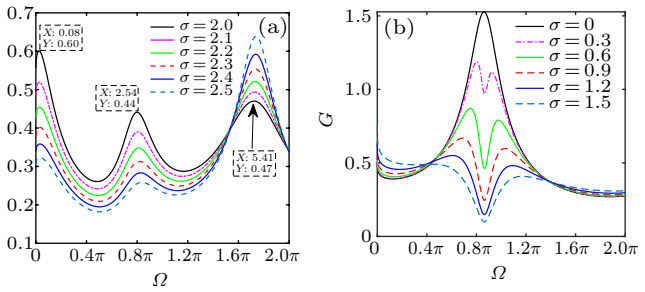


Fig. 24. PR phenomenon of $G(\Omega)$ with different values of noise amplitude σ under different parameters: (a) $\omega = 0.8$, $\lambda = 0.3$, $\alpha = 0.5$, $\tau = 1$; (b) $\omega = 2$, $\lambda = 0.5$, $\alpha = 0.3$, $\tau = 1$.

6. Conclusion

This paper focuses on a fractional-order globally coupled system with time delays and fluctuating frequency. In the theoretical solution aspect, we first utilize the time-delay decoupling formula and the fractional-order Shapiro–Loginov formula to establish the statistical synchronization of particle behaviors in the system, indicating that the mean field of the system is statistically equivalent to the individual particle behavior. Furthermore, based on this synchronization, two kinds of theoretical expression of output amplitude gains G and $\bar{G}$ are derived by time-delay decoupling formula and small delay approximation theorem, respectively. In the numerical simulation aspect, we employ the power series expansion method to numerically simulate the model and analyze the convergence of the algorithm with respect to simulation parameters. Based on the simulation algorithm, the accuracy of theoretical results G and $\bar{G}$ is analyzed. The analysis shows that as the τ increases, the error $G_{\text{num}} - \bar{G}$ gradually increases, while the error $G_{\text{num}} - G$ remains stable. This means that compared to $\bar{G}$, G is an exact theoretical solution, which means that G is not only more accurate in the region of small delay, but also applies to the region of large delay.

The collective dynamics behavior of particles, encompassing stability, synchronization, and resonance phenomena are presented, utilizing both theoretical analysis and numerical simulations.

To begin with, the system's statistical synchronization is demonstrated and corresponding synchronization conditions are provided. The statistical synchronization of particles ensures that the system's mean field behavior aligns statistically with the individual particle behavior. Consequently, by investigating the behavior of individual particles, we can effectively comprehend the collective behavior of the system. And this property is utilized to solve the particles' OAG. In the numerical simulation, the effect of damping force and coupling force on the synchronization is given. The results reveal nonlinear effects of damping force on synchronization, where the fractional-order α can either enhance or weaken synchronization depending on other system parameters. Without considering the coupling delay, the coupling force makes the particles attract each other. And as the coupling intensity ε increases, the coupling force increases, leading to the speed of synchronization increase. While by considering the coupling delay, in the motion of particles, the coupling force makes the particles attract or repel each other, which means the effect of the ε on the synchronization is nonlinear. And with different the value of ε, the increasing $\hat{\tau}$ may enhance or weaken the synchronization of the system.

In addition, the paper presents the stability condition of the system, revealing that the system remains stable as long as the noise amplitude σ is within a certain threshold. Moreover, it is observed that the stability region widens as the values of α and τ increase. Furthermore, it is concluded that when the system achieves stability, it ensures the statistical synchronization of particles.

Finally, based on these two distinct resonance mechanisms, we discuss three categories of resonance phenomena in the system: CSR, GSR, and PR. According to the SR mechanism, the phenomenon of SR aries from the optimal match achieved through the competition between order and randomness under nonlinear conditions. Besides, we also investigated the GSR phenomenon of $G(\Omega)$ and $G(\tau)$. According to the PR mechanism, PR occurs when there is a periodic matching between Ω and τ. Under the parameter settings without noise, analysis showed that when the relationship between Ω and τ satisfies $\Omega\tau + \alpha\pi/2 = \pi + 2k\pi, k = 0, \pm1, \pm2, \ldots$, the resonance peak of $G(\Omega)$ and $G(\tau)$ appears periodically. When system is affected by the noise, the occurrence of resonance phenomenon under the combined influence of the SR and PR mechanisms is explored. Analysis showed that the periodic matching between Ω and τ remains unaffected by the other parameters, ensuring the persistence of PR phenomenon. However, the presence of noise affects the period of $G(\tau)$ and $G(\Omega)$. Therefore, PR will not disappear, and when combined with the randomness introduced by the noise, the superposi-

tion effect of PR mechanism and SR mechanism results in a more diverse multi-peak resonance phenomenon.

In summary, the collective dynamics of fractional-order globally coupled systems with delays and fluctuating frequency is deeply studied in this study, and a series of important theoretical and experimental discoveries are made. While this paper primarily concentrates on a specific fractional-order differential model, the methodologies presented possess broad applicability. Future studies can further explore the systems with different noise sources, different coupling modes, and different orders (such as second-order differential system), and expand the research scope to further improve the understanding and application of the behavior of fractional-order coupled systems.

Appendix A: Analytical expressions of A, A_ξ, φ, and φ_ξ

In the limit of infinite time ($t \to \infty$), the functions $H_{ik}(t)$ approach zero, and the effect of initial conditions becomes negligible. Hence, it is assumed that the initial conditions are zero. In this case the mean particle displacement $y_1(t) = \langle x_i(t)\rangle$ is provided by

$$\langle x_i(t)\rangle = A_0 \int_0^t H_{10}(t-t')\cos(\Omega t')\,\mathrm{d}t'. \tag{A1}$$

$y_2(t) = \langle \xi(t) x_i(t)\rangle$ is given by

$$\langle \xi(t) x_i(t)\rangle = A_0 \int_0^t H_{20}(t-t')\cos(\Omega t')\,\mathrm{d}t'. \tag{A2}$$

In accordance with the theory of linear time-invariant systems, it can be inferred that

$$\langle x_i(t)\rangle = A\cos(\Omega t + \varphi), \tag{A3}$$
$$\langle \xi(t) x_i(t)\rangle = A_\xi \cos(\Omega t + \varphi_\xi), \tag{A4}$$

where

$$A = |\hat{H}_{10}(\mathrm{j}\Omega)|, \quad \varphi = \arg(\hat{H}_{10}(\mathrm{j}\Omega)),$$
$$A_\xi = |\hat{H}_{20}(\mathrm{j}\Omega)|, \quad \varphi_\xi = \arg(\hat{H}_{20}(\mathrm{j}\Omega)). \tag{A5}$$

According to analytical expression of $\hat{H}_{10}$ and $\hat{H}_{20}$ which can be determined in Eq. (25), we can get the analytical expressions of A, A_ξ, φ, and φ_ξ as follows:

$$\begin{cases} A = A_0\sqrt{\dfrac{{u_1}^2+{u_2}^2}{{u_3}^2+{u_4}^2}}, \\ \varphi = \arctan\left(\dfrac{u_2u_3-u_1u_4}{u_1u_3+u_2u_4}\right), \end{cases}$$
$$\begin{cases} A_\xi = A_0\sqrt{\dfrac{{u_1'}^2+{u_2'}^2}{{u_3}^2+{u_4}^2}}, \\ \varphi_\xi = \arctan\left(\dfrac{u_2'u_3-u_1'u_4}{u_1'u_3+u_2'u_4}\right), \end{cases} \tag{A6}$$

where

$$\begin{aligned} u_1 &= b^\alpha\cos(\theta\alpha) + \omega\mathrm{e}^{-\lambda\tau}\cos(\Omega\tau), \\ u_2 &= b^\alpha\sin(\theta\alpha) - \omega\mathrm{e}^{-\lambda\tau}\sin(\Omega\tau), \\ f_1 &= \Omega^\alpha\cos\left(\frac{\pi}{2}\alpha\right) + \omega\cos(\Omega\tau), \\ f_2 &= \Omega^\alpha\sin(\frac{\pi}{2}\alpha) - \omega\sin(\Omega\tau), \\ f_3 &= \sigma^2\mathrm{e}^{-\lambda\tau}\cos(2\Omega\tau), \quad f_4 = \sigma^2\mathrm{e}^{-\lambda\tau}\sin(2\Omega\tau), \\ u_3 &= f_1u_1 - f_2u_2 - f_3, \quad u_4 = f_1u_2 + f_2u_1 + f_4, \\ u_1' &= -\sigma^2\cos(\Omega\tau), \quad u_2' = \sigma^2\sin(\Omega\tau), \\ b &= \sqrt{\Omega^2+\lambda^2}, \quad \theta = \arctan\frac{\Omega}{\lambda}. \end{aligned} \tag{A7}$$

Appendix B: OAG without noise

Assuming no noise in the model, then there is no random part in the system. Because of synchronization, The model becomes as

$$\frac{\mathrm{d}^\alpha x_i(t)}{\mathrm{d}t^\alpha} + \omega x_i(t-\tau) = A_0\cos(\Omega t), \quad i = 1,2,\ldots,N. \tag{B1}$$

Using the fractional Shapiro–Loginov formula on the equation, the analytical expression of $x_i(t)$ is given as

$$x_i(t) = A_\mathrm{r}\cos(\Omega t + \varphi_\mathrm{r}), \tag{B2}$$

where

$$A_\mathrm{r} = \frac{A_0}{\sqrt{\Omega^{2\alpha}+\omega^2+2\omega\Omega^\alpha\cos(\Omega\tau+\pi\alpha/2)}},$$
$$\varphi_\mathrm{r} = \arctan\frac{\omega\sin\Omega\tau - \Omega^\alpha\sin\pi\alpha/2}{\omega\cos\Omega\tau + \Omega^\alpha\cos\pi\alpha/2}.$$

Therefore, the corresponding output amplitude gain is

$$G_\mathrm{r} = \frac{1}{\sqrt{\Omega^{2\alpha}+\omega^2+2\omega\Omega^\alpha\cos(\Omega\tau+\pi\alpha/2)}}. \tag{B3}$$

According to the expression of G_r, we can conclude that when

$$\Omega\tau + \frac{\pi}{2}\alpha = \pi + 2k\pi, \quad k = 0,\pm1,\pm2,\ldots \tag{B4}$$

satisfied, G_r gets the maximum value. This means that as the value of Ω (τ, α) changes, $G_\mathrm{r}(\Omega)$ ($G_\mathrm{r}(\tau)$, $G_\mathrm{r}(\alpha)$) will periodically reach its maximum value.

Acknowledgement

Project supported by the Natural Science Foundation of Sichuan Province, China (Youth Science Foundation) (Grant No. 2022NSFSC1952).

References

[1] Gammaitoni L, Hänggi P, Jung P and Marchesoni F 1998 *Rev. Mod. Phys.* **70** 223
[2] Benzi R, Sutera A and Vulpiani A 1981 *J. Phys. A* **14** L453
[3] Stroescu I, Hume D B and Oberthaler M K 2016 *Phys. Rev. Lett.* **117** 243005
[4] Duan F, Pan Y, Chapeau-Blondeau F and Abbott D 2019 *IEEE Trans. Signal Process* **67** 4611
[5] Mcnamara B and Wiesenfeld K 1989 *Phys. Rev. A* **39** 4854
[6] Cubero D 2008 *Phys. Rev. E* **77** 021112
[7] Jian L, Bing H, Fan Y, Chuan L Z and Xiao J D 2020 *Commun. Nonlinear Sci. Numer. Simulat.* **85** 105245
[8] Gammaitoni L, Marchesoni F, Menichella-Saetta E and Santucci S 1994 *Phys. Rev. E* **49** 4878
[9] Li JH 2002 *Phys. Rev. E* **66** 031104
[10] Berdichevsky V and Gitterman M 1996 *Europhys Lett.* **36** 161
[11] Gitterman M 2005 *Physica A* **352** 309
[12] Yu T, Zhang L and Luo M K 2013 *Phys. Scr.* **88** 045008
[13] Nicolis C and Nicolis G 2017 *Phys. Rev. E* **96** 042214
[14] Tu Z, Zhao D Z, Qiu F and Yu T 2020 *J. Stat. Phys.* **179** 247
[15] Jiang L, Lai L, Yu T and Luo M K 2021 *Acta Phys. Sin.* **70** 130501 (in Chinese)
[16] Quintero-Quiroz C and Cosenza M G 2015 *Chaos, Solitons and Fractals* **71** 41
[17] Massihi N, Parastesh F, Towhidkhah F, Huihai W, Shaobo H and Jafari S 2024 *Europhys. Lett.* **146** 21005
[18] Zhong S C, Zhang L, Wang H Q, Ma H and Luo M K 2017 *Nonlinear Dyn.* **89** 1327
[19] Raúl V S 2023 *Commun. Nonlinear Sci. Numer. Simulat.* **117** 106934
[20] Lin L F, He M Y and Wang H Q 2022 *Chaos, Solitons and Fractals* **154** 111641
[21] Liang X M, Tang M, Dhamala M and Liu Z H 2009 *Phys. Rev. E* **80** 066202
[22] Zou W, Senthilkumar D V, Tang Y, Wu Y, Lu J Q and Kurths J 2013 *Phys. Rev. E* **88** 032916
[23] Zhong Y F, Luo M K, Chen X and Yu T 2024 *Commun. Nonlinear Sci. Numer. Simulat.* **130** 107799
[24] Zeitler M, Daffertshofer A and Gie-len CCAM 2009 *Phys. Rev. E* **79** 065203
[25] Majer N and Schöll E 2009 *Phys. Rev. E* **79** 011109
[26] Borromeo M and Marchesoni F 2007 *Phys. Rev. E* **75** 041106
[27] Roxin A, Brunel N and Hansel D 2005 *Phys. Rev. Lett.* **94** 238103
[28] Wang Q Y, Perc M, Duan Z S and Chen G R 2009 *Phys. Rev. E* **80** 026206
[29] Banerjee T, Biswas D and Sarkar BC 2013 *Nonlinear Dyn.* **71** 279
[30] Banerjee T and Biswas D 2013 *Nonlinear Dyn.* **73** 2025
[31] Banerjee T, Biswas D and Sarkar BC 2013 *Nonlinear Dyn.* **72** 321
[32] Wang F, Zhang C and Li L 2023 *Commun. Nonlinear Sci. Numer. Simulat.* **126** 107447
[33] Stamova I, Stamov G and Li XD 2023 *Fractal Fract.* **7** 845
[34] Lin L F, Lin T Z, Zhang R Q and Wang H Q 2023 *Chaos, Solitons and Fractals* **170** 113406
[35] Yu T, Zhang L, Ji YD and Lai L 2019 *Commun. Nonlinear Sci. Numer. Simulat.* **72** 26
[36] Yan Z, Guirao J L G, Saeed T and Liu X B 2022 *Nonlinear Dyn.* **110** 1233
[37] Zhang G C and Li J H 2010 *Commun. Theor. Phys.* **53** 303
[38] Fang Y W, Luo Y and Zeng C 2022 *Chaos, Solitons and Fractals* **155** 111775
[39] He L F 2023 *Phys. Scr.* **98** 035207
[40] Shapiro V E and Loginov V M 1978 *Physica A* **91** 563
[41] Kempfle S, Schafer I and Beyer H 2002 *Nonlinear Dyn.* **29** 99
[42] Guillouzic S, L'Heureux I and Longtin A 1999 *Phys. Rev. E* **59** 3970
[43] Kim C, Lee E K and Talkner P 2006 *Phys. Rev. E* **73** 026101